MÉRNÖKI ÉS INFORMATIKAI MEGOLDÁSOK

ENGINEERING AND IT SOLUTIONS

EÖTVÖS LORÁND UNIVERSITY
FACULTY OF INFORMATICS
SAVARIA INSTITUTE OF TECHNOLOGY

II. 2021.

MÉRNÖKI ÉS INFORMATIKAI MEGOLDÁSOK
ENGINEERING AND IT SOLUTIONS

II. 2021.

IMPRESS

Publisher
Eötvös Loránd University, Faculty of Informatics
Savaria Institute of Technology
Prof. Dr. László Kollár, head of institute

Cover design
Dr. Ferenc Safranyik

HU ISSN 2677-1691

HU-9700, Szombathely, Károlyi Gáspár tér. 4.
Contact: sf@inf.elte.hu, URL

TABLE OF CONTENTS

Application of 3D printing in casting

Márton Tamás Birosz[a], Kristóf Ferenczy[b], Mátyás Andó[c*]

[a] *ELTE, Faculty of Informatics, Savaria Institute of Technology, PhD student*
[b] *ELTE, Faculty of Informatics, Savaria Institute of Technology, Mechanical Engineering MSc, II. year*
[c] *ELTE, Faculty of Informatics, Savaria Institute of Technology, associate professor*

ABSTRACT

The article presents the applicability of 3D printing in casting. Even complex models produced by 3D printing can be effectively applied in the field of lost pattern casting. The process was realized using Polycast and Pioneer investment powder (gypsum). Based on the measurement it is clear that the size differences come from the printing technology. The minimum wall thickness cannot be less than 0.8 mm, but there is inaccuracy under 2.1 mm when there is no infill section in the rib. More contour lines can reduce the deformation and the inaccuracy.

Keywords: *Lost pattern casting, Tin casting, 3D printed models*

1. Introduction

Whether in the automotive or mechanical engineering industries, the development or small-scale production of complex components such as gearboxes and other parts of the driveline must be fast and efficient [1]. Precision casting using the conventional wax pattern used in the past has several weaknesses in this regard. Because metal printing is still relatively immature today, most companies still use wax-patterned [2] or plastic printed pattern for casting [3, 4]. In previous wax-patterned precision casting, in many cases, the immediate production of the desired wax models was a problem because it required expensive injection molding tools and wax presses.

These tools can be almost prohibitively expensive and time consuming when needed for small series or upgrades, resulting in very high unit prices [5]. Today, wax pattern are being replaced widely by pattern, which made by 3D-printing. Manufacturing plastic pattern with 3D printing is very simple, accurate and fast. No tools are required as the printing process is based on the CAD data of the part. The 3D printer produces the pattern by layer-by-layer construction method with excellent repeatability and performance, no matter how complex the part itself. Constructions designs can go beyond current manufacturing processes, and changes are extremely simple by resubmitting CAD data [6, 7]. The casting method used in this research belongs to the lost pattern casting, within that the casting was realized with gypsum mold.

Traditionally, a precision metal pattern is used for gypsum mold casting. Gypsum mold material is poured, then after removing the pattern, the cavity of the product is formed. After the gypsum mold has hardened, it is advisable to remove the residual moisture content from the mold by a heat treatment. The resulting mold usually consists of two parts, because the undercut of the parts requires the use of dividing planes [8]. The whole process is illustrated in Fig. 1.

*Corresponding author: Mátyás Andó, am@inf.elte.hu
https://doi.org/10.37775/EIS.2021.2.1

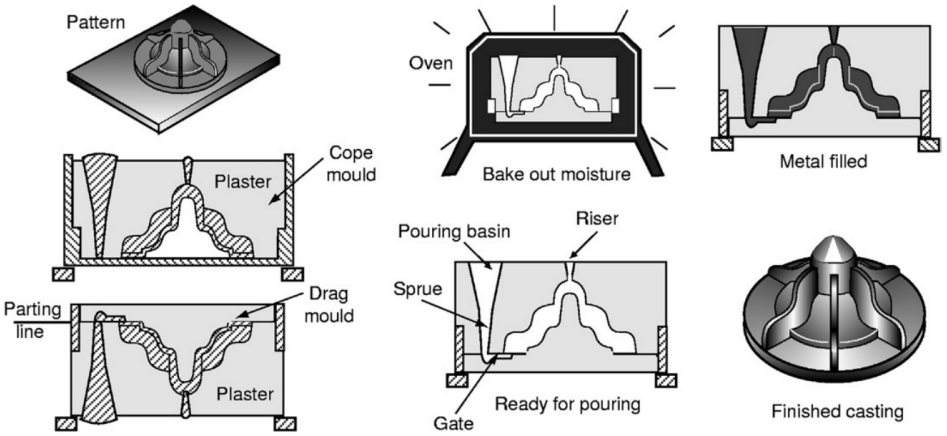

Figure 1. Plaster mould casting [8]

To avoid the parting line the accuracy can improve. Evaporative-pattern casting (lost-foam casting) one of the solution to eliminate the parting line. This case the mold is produced by pouring the mold material around the pattern. Then, the pattern evaporates by burning out and thus the mold cavity is formed [9]. Fig. 2 illustrates lost pattern casting [8]. Moreover with lost pattern casting, it is possible to cast more detailed and complex geometries, as it is much simpler and more cost-effective to produce the pattern, and unlike casting into plain sand, there are no restrictions on the parting line [10]. In this article, lost pattern casting was implemented using 3D printing, which combines the benefits of additive manufacturing technology with casting.

2. Materials and methods

For the study, a FDM printer and "Polycast" brand filament were used. This material soften at 73 °C for casting and burn without residue at temperatures above 600 °C. The main properties and the suggested printing parameters of Polycast are in Table 1.

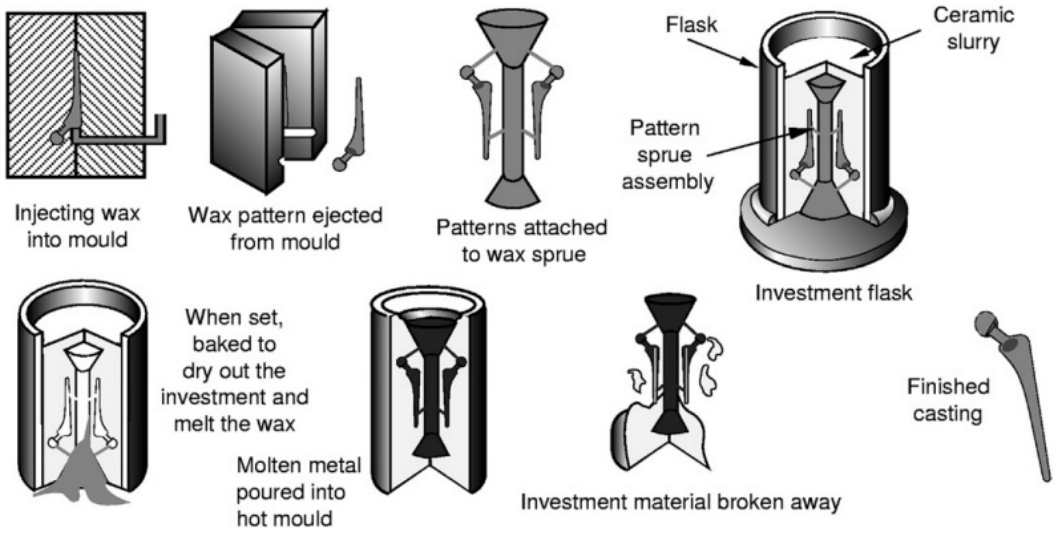

Figure 2. Wax-based – lost pattern casting [8]

Table 1. Polycast filament properties [11]

Property	Typical Value
Density (ρ), [g/cm^3]	1.1
Glass transition temperature (T_g), [°C]	70
Vicat softening temperature (T_v), [°C]	67
Young's modulus (E), [MPa]	1 745
Tensile strength (R_m), [MPa]	35.7
Elongation at break (ε), [%]	6.9
Nozzle temperature (T_n), [°C]	220
Build plate temperature (T_p), [°C]	60
Printing speed (v), [m/s]	50

For printing a Prusa I3 MK3 MMU2S printer was used and 0.2 mm layer thickness has been set. For printing temperatures and speed, the recommended values were used from the table (Table 1). The infill percentage was the minimal 20%. In the present case, the mechanical properties were not the key question, but minimal amount of material should be preferred. Thanks for this, the next technology step is become much easier.

Pioneer investment powder (gypsum), Crystalline Silica CAS 14808-60-7 composition 70-80%, has been used to create the mold [12]. The mouldable material was formed by mixing the powdered material with water in a ratio of 2.5:1. The mold material can be molded for 10 minutes and then solidified. After solidification, it is advisable to wait 24 hours for the already solidified material to reach the desired strength.

SN99 (Table 2) was used to the raw-material of the casted parts, which contained 0.04% silver and 0.06% copper as impurities.

3. The developed casting process

The goal was to make parts with complex surfaces by casting. The selected sub-type casting was the lost pattern method. The parts do not require support when printing because of the selected casting technology. With this solution small burrs can avoid because there is no support removing process. Not only just the mold can be created easier, but the accuracy and the surface quality are also greater.

In principle, PLA plastic is also suitable for printing the form. However, it is advisable to use a vacuum chamber during firing, as inappropriate conditions the PLA will not evaporate but will char and burn on the mold cavity wall. This making the molded product inaccurate and contaminated [14]. So the pattern has been made from Polycast filament material (Step #1). Polycast filament material has the advantage of completely evaporating at $T > 600$ °C. This way the product will not be contaminated and free of inclusions. The mold is made of Pioneer Investment Powder gypsum

Table 2. Tin properties [13]

Property	Typical Value
Density (ρ), [g/cm^3]	7.4
Tensile strength (R_m), [MPa]	22
Elongation at break (ε), [%]	41
Melting point (T_m), [°C]	227

Figure 3. Casting error because of the rapid solidification

(Step #2), which has a high heat shock resistance. Due to its fine grain size, can be used to produce accurate products. When preparing the mold, it is important to adhere to the mixing ratio (2.5:1), otherwise a mixture of acceptable hardness will not be obtained and the mold may crack during firing. The gypsum mold must be allowed to stand for 24 hours until it reaches the required strength. The printed pattern was completely covered by casting gypsum.

It is advisable to place the crucible upside down in the oven so that the plastic that has become liquid at the beginning can flow out from the mold (Step #3). As the furnace only heated up to 600 °C. Although the plastic completely evaporates at high temperatures, it initially becomes only liquid. Based on our experience, to remove the liqiud plastic from the mold can gives better quality. In this case, it takes less time to burn out the polymer. If we do not wait long enough for firing, it will not evaporate completely and remains at the bottom of the mold.

The tin (SN99) has a good shape-filling ability and has a low shrinkage even after casting [15]. Particular care should be taken when casting liquid metal into a mold because the load of the flowing metal can damage the fired surface of the mold. This can be eliminated primarily by proper design and construction of the gating system and the right casting speed. Our case, the pouring cup is

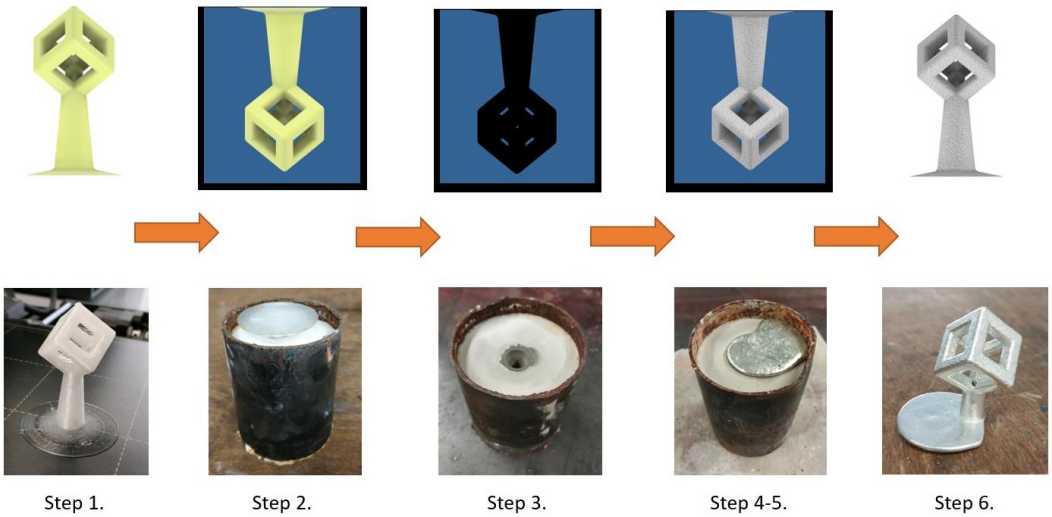

Figure 4. The casting process

made integral with the component. When preparing the sample, it is advisable to achieve the correct orientation of the model. This was extremely important in the casting (Step #4), because after the melting of the casting material, the surface of the bulk material solidified relatively quickly at room temperature. Thus, during molding, the already frozen material leads to surface defects and uneven filling. Fig. 3 shows the effect of the rapid solidification and the presence of impurities affect the quality of the casting. After casting, the metal must be allowed to cool down (Step #5). Then the gypsum mold can be completely washed out form the parts with high-pressure water (Step #6), so that the molded sample is not damaged. Fig. 4 shows the implementation (Step #1 to Step #6), from the design of the plastic model to the finished molded model.

4. Casting accuracy, technological limits

It can be seen in Fig. 4 that the construction of the relatively complex lattice structure was not an obstacle either. One of the advantages of the method to be emphasized is that such a mold could be difficult to implement when casting with a sand mold due to the undercuts. Next to the complex shape there are two parameters which determine the casting possibility: one is the difference between the pattern and the final product, the other is the minimum wall thickness.

To do evaluate these properties, a special specimen was designed. The pattern contains ribs of different wall thicknesses, they were placed evenly distributed around the inlet opening. Thus ensuring that the ribs of different wall thicknesses had an equal chance of filling and that the metal could cool evenly in the mold cavity. The Fig. 5 illustrates the model and the finished casting.

It can be seen the finished piece that air bubbles trapped on the mold, which creates spikes (marking with red in Fig. 5) of the casted part. The casted piece shows a larger burr at the bottom (top in Fig. 5) of the ribs, the reason of this the printing technology. The adhesion has to increase with the printing tray with the fitted skirt. If the skirt could not be completely removed the burrs appear of the casted part also. Take account, if the skirt not removed completely, the metal parts

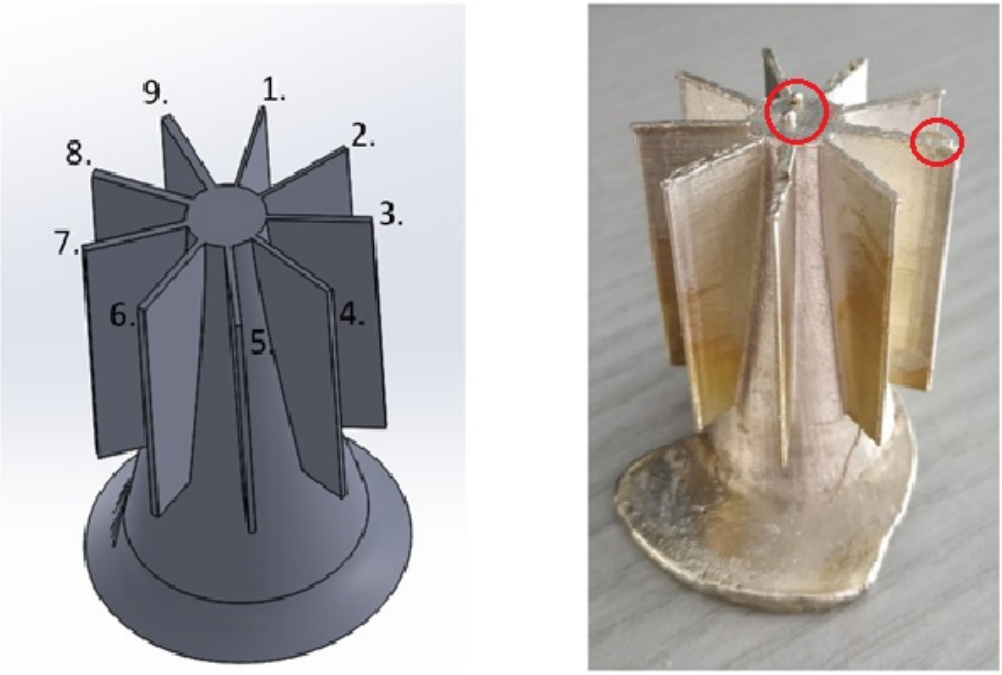

Figure 5. Specimen with ribs and the casted metal part

become bigger. Most of the case, the metal can deburr much easier so with material removing the casted part become in the tolerance zone. Apart from these, the sample is perfectly suitable for carrying out the measurement, as neither inclusion nor other deformities were formed. After the first sample, another sample has been manufactured with bigger rib thicknesses.

Each rib was measured on the 3D printed sample and on the casted piece as well. A digital caliper was used at several points along the length of the rib. The wall thickness of the 1st rib is 0.5 mm, then that of the subsequent ribs always increases by 0.1 mm. By measuring the individual ribs along their length in several places, it was found that the shrinkage or casting direction during casting did not adversely affect the dimensions, and the thicknesses have an acceptable tolerance within the entire surface. By plotting the measured values graphically, the differences are striking and the conclusions can be drawn more easily. The upper part of Fig. 6 shows the measured data. Based on the diagram, it can be said that the difference between the dimensions of the printed sample and the dimensions of the CAD model is larger than between the dimensions of the printed sample and the casted part.

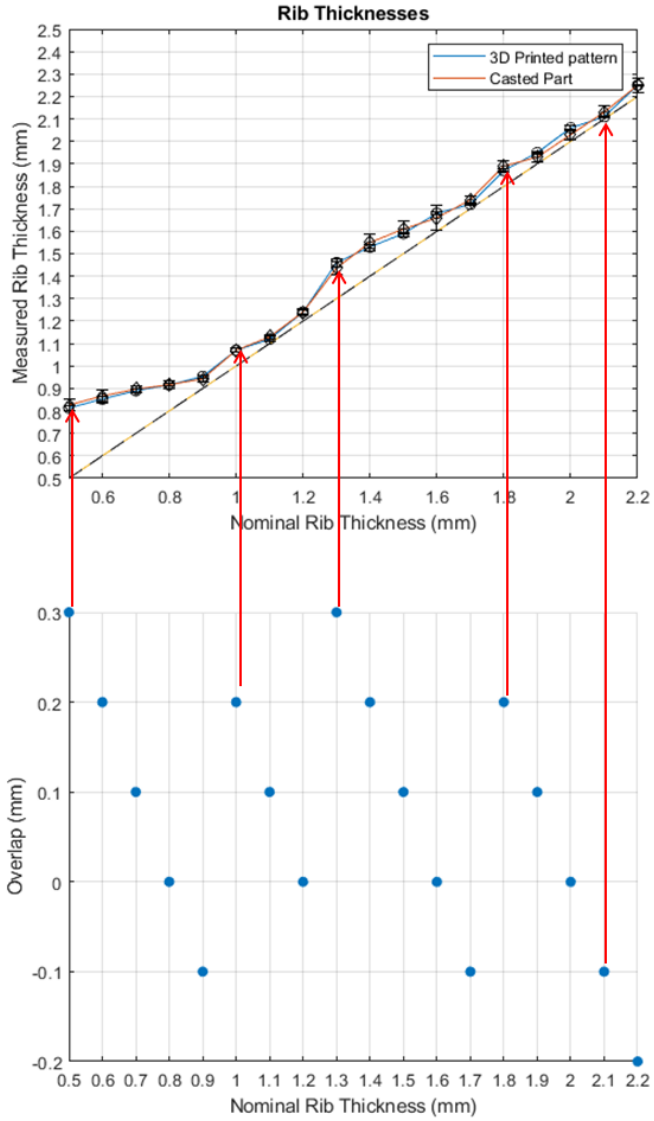

Figure 6. Measured data

There is almost no difference between the printed sample and the cast part, only 10-20 μm differences was recorded. This was the same as the range of the inaccuracy of the caliper. Thus, it can be said that the lost pattern casting can be realized from a 3D printed pattern is functional and can be carried out with high accuracy. Possible size problems are only comes from the inaccuracy of the printing process. The lower part of Fig. 6 shows the overlap value for each rib, which is a manufacturing feature, which involved in the next chapter.

5. Inaccuracy of FDM printing

Bigger difference only occurs for thinner walls (under 0.9 mm), which can be traced back to the FDM printing technology. The 3D printer use a nozzle with 0.4 mm diameter hole which it extrudes the plastic filament. Consequently, if the setting parameters are optimal, both the extruded and the deposited fiber should be at least 0.4 mm thick (Fig. 7/a). Sometimes, because of the thin layer thickness, the print head may deform the deposited fiber (Fig. 7/b) due to the narrow gap thickness, so its width may increase. Also the overlapping fibers cannot be mixed together in this way either, as they suffer from plastic deformation. Fig. 7/c shows the simplify real cross section with deformation in case thin layer and overlapping of the extruded lines.

The material leaving the extruder will undergo a plastic deformation due to the pressure change, so the diameter of the extruded material will not be the same as the diameter of the extruder, but will be slightly wider [16]. The software tries to maintain the nominal size by printing adjacent contour lines closer together, but this results a theoretical overlap within a layer and then smears

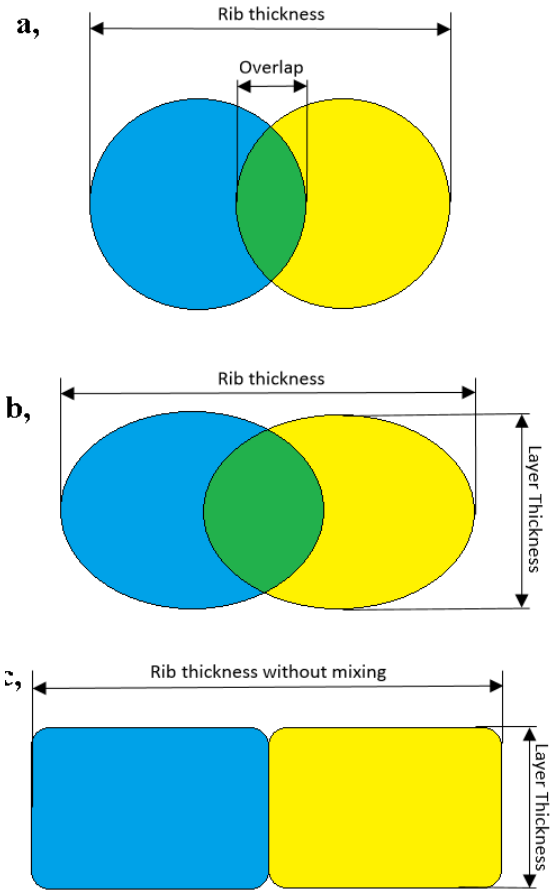

Figure 7. Cross section of the extruded lines a) nominal b) compressed c) deformed

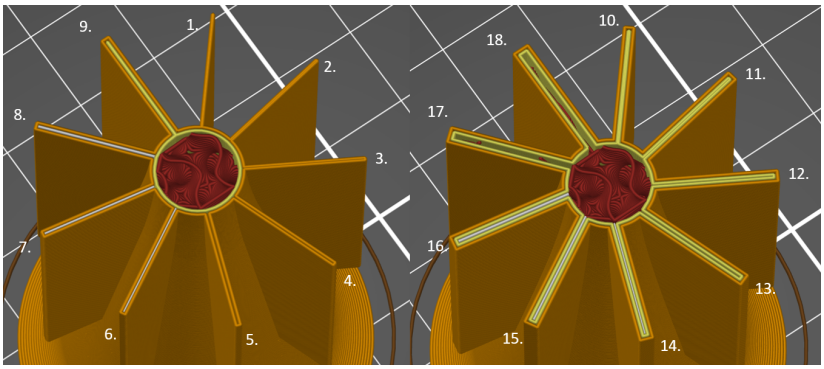

Figure 8. The generated toolpath

it in the plane of the printer head when the next layer is formed. Based on these phenomenon, the given thickness of printed part can be only bigger than 0.4 mm.

But the thickness not only affected of extruded filament size but also the printing path. The created surface model is opened in the printer's slicing program and sliced with the usual parameters to show the created toolpath. The generated toolpath is shown in Fig. 8. The FDM printing technology always start to print the contour of the layer. In our case it was only one contour line (which is the minimum), but in case of ribs that is means two printed filament next to each other (clearly seen in Fig. 8 the rib 3-7). In reality, however, it first draw a given layer of parts with a contour line and then infill the surface bounded by the contour line according to the infill pattern and density percentage.

Since the infill pattern is not parallel to the contour lines, it does not apply that its size. So the size can only be a multiple of the thickness of the contour line for thin walls. The part is at least as thick or thicker than the contour lines, the part will be finished close to the nominal size. In the present case, however, ribs numbered 1-3. have smaller thickness than the two contour lines together, they cannot be thinner than 0.8 mm.

To understand more the size effect, the printed path was examined in more detailed. In the present case, the contour line embodies the right and left sides of the ribs. When drawing the middle cylindrical part, it begins to extrude one side by layer, then reaching the end of the rib, extruding the outer surface of the rib by a perpendicular displacement and then extruding the other side of the rib moving backwards. Even perpendicular displacement is small, at constant speed the volume also constant, so the rib cannot be smaller (Fig. 7/c). The perpendicular displacement gives the overlap. Overlap of 0 mm (the perpendicular displacement is 0.4 mm) means the two contour lines are right next to each other, while an overlap with a negative value is a gap between the two contour lines.

This explains why there is such a difference between the curves at the beginning in Fig. 6. Interestingly, rib 1. apparently consists of a single contour line, which would be logical, as its nominal size is only 0.1 mm larger than the thickness of the contour line, but in order for the layer to print continuously, the print head reaching the tip of the rib does not interrupt the extrusion with a high-speed motion, but also extrudes the material backwards, barely moving in the perpendicular direction. So in this case also two outer contour lines have been created.

From the measurement results, it can be seen that when printing the ribs, the duplex line results in a thickness of at least 0.8 mm. In fact, when the tracks are printed so close together that the material extends sideways. It can be observed that 1-5. for ribs, the software draws only the outer contour lines with the extruder and starts extruding the inner contour lines only at rib 6, as it can been seen .As the nozzle moves more and more between the two outer tracks, the thickness also increases slightly. It can be seen in Fig. 8 that rib 5 (0.9 mm thick) develops a state where the

printed contour fills the space so that it is nearly identical to the CAD model. Since the value of the overlap is negative for this rib, no deformation per layer will occur, which explains the accuracy.

For ribs thicker than 0.9 mm but 1.2 mm thinner, outer contour lines and the inner contour lines are also present. Three lines, two outer contours and one inner contour line, are drawn next to each other. However, because the extruder can print a line at least 0.4 mm thick, it prints the inner contour line on the outer contour line for a fill space of less than 0.4 mm. For this reason, the same consequence occurs as for the previously mentioned thin ribs (up to a rib thickness of less than 0.9 mm). There is a further difference between the 1.2 and 1.7 mm thick ribs. But the 1.7 mm thicker ribs are already approaching the nominal size and are made with the same inaccuracy. In the case of ribs with a thickness of 1.7 mm, the effect of the adjacent lines extruded on each other is still significant. However, for thicker wall thickness (1.8–2.0 mm ribs), this effect is less significant.

Thicker ribs create more contour lines, which reduces this error. This is because the outer contour is created first, i.e. there is no shortage of space and the contour lines start to solidify in the correct position. When the inner contour lines are printed, they squeeze the outer layer. When last contour line is inserted (which fill the rest), the stiffer outer part can change the size much smaller. Actual infilling (with pattern and density) can only be observed for the last two ribs. The size of these ribs is also close to the nominal size, so it can be assumed that thicker ribs also have such accuracy. The highest accuracy is achieved when the nominal size is a multiple of the extruded line or it is thicker than 2.0 mm. The last two ribs no longer affected by this phenomenon, because there is infill inside the rib. From this point, the accuracy of the printer will determine the actual size. The lower part of Figure 6 shows the overlaps depend from perpendicular displacements. It is clear that the size curves are broken when the printing strategy changes (marked with arrows). The slicing program always tries to have more overlap (rib thicknesses of 0.5, 1, 1.3, and 1.8 mm), however, the volume is still constant, so the wall thickness cannot actually decrease.

6. Conclusions

Metal printing is still extremely expensive these days, additive loss pattern casting is preferred in practice as an alternative, low-cost solution. In this article, the feasibility study of Additive Loss Pattern Metal Casting was presented. The Loss Pattern was made from Polycast filament sample material, and the mold was made with special plaster (Pioneer Investment Powder). The casting was formed by casting molten metal (SN99) into the mold cavity previously burn out the polymer pattern and then removing the gypsum mold.

After establish the new casting process, a special specimen was designed to evaluate the accuracy. The ribs of different wall thicknesses were printed from polymer and then the mold required to cast the tin was made. We found that the dimensions of the printed and cast parts show a negligible difference, while the dimensions of the CAD model already showed a more significant difference compared to the printed part.

While exploring the causes, we found that the print path plays a key role in the error. Based on these, the following was found when printing thin ribs:

- at least two contour lines are made in case of one rib, so the thickness of the rib must not be less than 0.8 mm,
- the slicing program tries to compensate for dimensional errors by overlapping (smaller perpendicular displacement), which is not a sufficiently efficient method,
- a rib consists of more contour lines, which lead smaller size error caused by printing,
- above 2.1 mm, where the infill already appear, the rib width error is depends on the accuracy of the printer.

7. Acknowledgement

Application Domain Specific Highly Reliable IT Solutions" project has been implemented with the support provided from the National Research, Development and Innovation Fund of Hungary, financed under the Thematic Excellence Programme TKP2020-NKA-06 (National Challenges Subprogramme) funding scheme.

8. References

[1] Gy. Falk, T. King, *Precíziós öntés 3D nyomtatással*, download date: 10. 10. 2020, url

[2] M. Horváth, *ANZDOC*, download date: 18. 9. 2020, url

[3] M.R. Nichols, *How does the automotive industry benefit from 3D metal printing?*, Metal Powder Report 74(5), 2019, pp. 257-258. CrossRef

[4] L. Gardner, C. Buchanan, *Metal 3D printing in construction: A review of methods, research, applications, opportunities and challenges*, Engineering Structures 180, 2019, pp. 332-348. CrossRef

[5] Á. Németh, Sasovits, *Öntészet*, download date: 5. 11. 2020, url

[6] B. Berman, *3-D printing: The new industrial revolution*, Business Horizons 55(2), 2012, pp. 155-162. CrossRef

[7] M. Attaran, *The rise of 3-D printing: The advantages of additive manufacturing over traditional manufacturing*, Business Horizons 60(5), 2017, pp. 677-688. CrossRef

[8] K.G. Swift and J.D. Booker, *Manufacturing Process Selection Handbook*, Oxford: Butterworth-Heinemann, 2013. CrossRef

[9] J. Campbell, G.W. Kuhlman. J.R. Grassi, *Lost Pattern Mold Removal Casting Methods and Apparatus (patent)*, 2005, download date: 19. 11. 2020, url

[10] T.S. Piwonka, A comparison of lost pattern casting processes, Materials & Design 11(6), 1990, pp. 283-290. CrossRef

[11] Lulzbot, *Polymaker*, download date: 18. 11. 2020, url

[12] SRS, *SRS Setting The Standard*, download date: 18. 11. 2020, url

[13] M.B. Ouvres, *mbv*, download date: 18. 11. 2020, url

[14] J. Flynt, *Polylactic Acid (PLA): The Environment-friendly Plastic*, 3DINSIDER, download date: 9. 11. 2020, url

[15] TheMetalCasting, *Tin Alloy*, download date: 9. 11. 2020, url

[16] T. Czvikovszky, P. Nagy, J. Gaál, *A polimertechnika alapjai*, Budapest, Műegyetemi Kiadó, 2007.

Investigation of the wear of rolls in asymmetric rolling

János György Bátorfi[a*], Purnima Chakravarty[b], Jurij Sidor[c]

[a] *ELTE, Faculty of Informatics, Savaria Institute of Technology, PhD student*
[b] *ELTE, Faculty of Informatics, Savaria Institute of Technology, PhD student*
[c] *ELTE, Faculty of Informatics, Savaria Institute of Technology, full professor*

ABSTRACT

In the present work, both symmetric and asymmetric rolling processes were investigated by means of numerical approaches. From the algorithm presented, values of rolling pressure and sliding velocity in the roll gap were determined. These variables allow the estimation of tribological parameters of a given material. To determine the wear of the rolls and rolled materials the Archard's law has been employed. Results of numerical simulations show that the quantitative characteristics of the wear reveal a slight change for slower roll. Whereas the wear value for the faster roll increases with an increase of roll velocity ratio. It was found that for a given roll velocity ratio, rise of friction coefficient causes insignificant change in the wear value for the slower roll, while this value tends to decrease rapidly for the faster roll.

Keywords: *Asymmetric rolling, Wear, Archard's law, Al alloys, FEM simulation*

1. Introduction

The industrial demand for flat product of metal and alloys is very high, which is basically obtained by the process of rolling. The rolling procedure can be divided into cold and hot rolling depending on the temperature maintained during the rolling process [1–3]. On the other hand, from the tribological aspect, rolling can be divided into the following groups: rolling with lubricant and dry rolling [1, 2, 4]. However, while applying lubricants [1], the viscosity of the lubricants bears an important part in the wear processes. From another point of view, the rolling process can be subdivided into two more categories such as symmetric and asymmetric rolling depending on the rolling conditions. The more common procedure is the symmetric rolling, where the relative velocities between the two rolls is identical throughout the process. On the other hand, in case of asymmetric rolling the rolls have different peripheral velocity. The advantage of using asymmetric rolling (ASR) over symmetric rolling is that the material suffers significant shear deformation, which cannot be introduced by the conventional rolling. At the same time, the disadvantage associated with the ASR is that the process parameters depend on the peripheral velocities and there is a significant slip between the rolls and the rolled material. It is possible to characterize the technique of ASR, in terms of roll velocity ratio K_V [5]:

$$K_V = \frac{V_{\max}}{V_{\min}}, \tag{1}$$

where, $V_{\max}$ is the peripheral velocity of the roll with a higher velocity and $V_{\min}$ is the peripheral velocity of the roll with a lower velocity.

*Corresponding author: János György Bátorfi, bj@inf.elte.hu
https://doi.org/10.37775/EIS.2021.2.2

It has been observed that, different models for determining the wear values for friction bodies are described in the literature. One of them is the Archard's law. This law is described by considering the amount of loss in volume due to sliding contact between two materials [6]. However, there is a modified form of the Archard-law [7] that deals with the pressure of contact instead of the original model that focuses on considering the force between the contact surfaces. The modified Archard law is given by Eq. (2), which has been used directly in Finite Element modeling to study the subject.

$$\frac{dh}{dt} = k \cdot p \cdot |dv| \tag{2}$$

In Eq. (2), dh/dt is the wear rate [mm/s]; k is the wear coefficient [mm^3/Nm] which can be treated as a material parameter; p is surface pressure between the bodies in contact at the point under test [MPa] and dv stands for sliding velocity at the test point [mm/s].

The described relation is not applicable in the initial and very advanced stages of wear [8]. The initial stage is the early short stage of wear, where small defects bulge out from the surface wear off, so that the wear coefficient value is significantly higher than the wear coefficient values for the subsequent stages. The Advanced stage is the step of the wear process where material fragments detached from the worn surface have a significant abrasive effect. In the initial stage, the wear coefficient may be several times higher than the values for the other stages of the process. The typical wear mechanism for a "Block-on-Ring" type sliding contact is adhesive wear according to [1, 8].

The current contribution aims to study the dry cold rolling process. While using Eq. (1), it has been considered that the radius and friction coefficient of the rolls are identical. Other parameters under consideration are the roughness of the rolls and the plate [2]. The effect of surface roughness is attributed in terms of the friction coefficient value, which is similar to the results presented in literature [2]. In case of employing Eq. (2), the effect of initial wear stages has been neglected. On the other hand, the advanced stage was assumed not to reach optimum stage of the wear process during the whole lifetime of the rolls.

2. Material and method

2.1. Material parameters and modelling

In order to investigate the phenomenon of wear of roll cylinders during both symmetric and asymmetric rolling, the commercially available Deform 2D finite element software [10] was employed. In the FEM calculations, the following technological and material parameters were used:

- The rolls were considered as rigid bodies with the diameter of 150 mm.
- The angular velocities of the upper and lower rolls were change between 1.1-2.2 rad/s.
- The calculations were performed for asymmetric ratios K_V ranging between 1-2.
- For the mechanical-strength parameters, the parameters of the material Al-6063 incorporated in the DEFORM-2D software were used [10].
- The initial thickness of sheet was 2 mm, while the final was 1.5 mm.
- The friction coefficient was changed in range from 0.075 to 0.25.
- The wear coefficient for aluminum (Al-6063) was $k_{Al} = 1 \cdot 10^{-5}$ mm^3/Nm.
- The wear coefficient for aluminum changes in the range of $k_{Al} = (0.5-1.5) \cdot 10^{-5}$ mm^3/Nm [8, 9].
- The wear coefficient for steel was $k_{St} = 5 \cdot 10^{-6}$ mm^3/Nm [8].

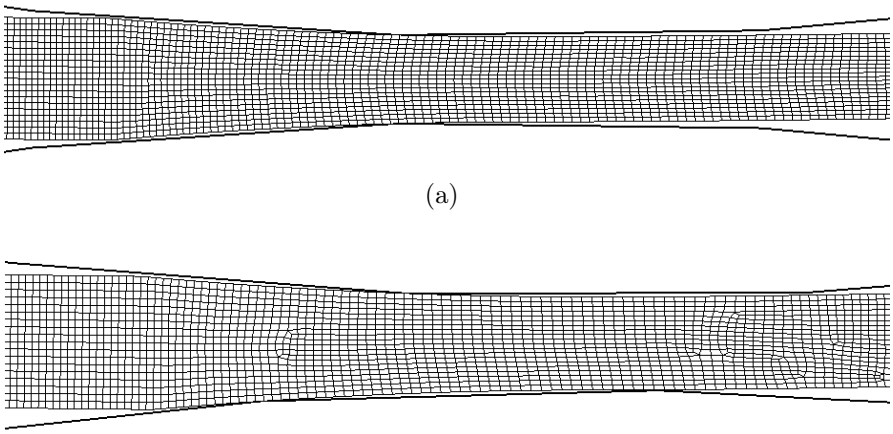

(a)

(b)

Figure 1. *a)* Partially deformed mesh for symmetric rolling (R=75 mm; ω=1.1 rad/s; h_i=2 mm; h_f=1.5 mm; μ=0.15), *b)* Partially deformed mesh for asymmetric rolling (R=75 mm; ω_b=1.1 rad/s; ω_t=0.748 rad/s; h_i=2 mm; h_f=1.5 mm; μ=0.15)

2.2. FEM modeling

The DEFORM 2D software was used to model the rolling process. The peripheral velocity and friction coefficient of the rolls were varied for the different rolling simulations. In all cases, the initial velocity was set to 1.1 rad/s. The modelling was done on a regular mesh of squares with equal time steps. The constructed, partially deformed mesh is shown in Fig. 1/a and Fig. 1/b.

3. Results

In the simulations represented, the effect of friction coefficient and velocity ratio were investigated for symmetrical and asymmetrical rolling with the same geometry. The model parameters are given in Table 1.

In the FEM model, the surface pressure and the sliding velocity were extracted for the lower and upper points of the plate at different time steps, and the wear value for the points was calculated by employing Eq. (2). An example of data extracted for symmetric rolling is shown in Fig. 2/a. The calculated $\int p \cdot |v| \, dt$ values for the different diagrams are signed by p. Fig. 2/a shows that in the case of symmetric rolling, the pressure and the relative sliding velocity values between the two rolls are nearly identical. The surface pressure at the inlet and outlet of the rolling gap is 0 MPa, with the maximum value at the contact point corresponding to a sliding velocity of 0 mm/s. As shown in Fig. 2/b, the increase in wear values is the same for the lower and upper points.

The extracted data for asymmetric rolling are presented in Fig. 3/a and Fig. 3/b shows that in contrast to symmetric rolling, the two rolls do not experience the same pressure and sliding velocity,

Table 1. Technological parameters used for FEM modelling

Parameter	**Value**
R, [mm]	75
ω_b [rad/s]	1.1
h_i [mm]	2
h_f [mm]	1.5
μ [-]	0.15

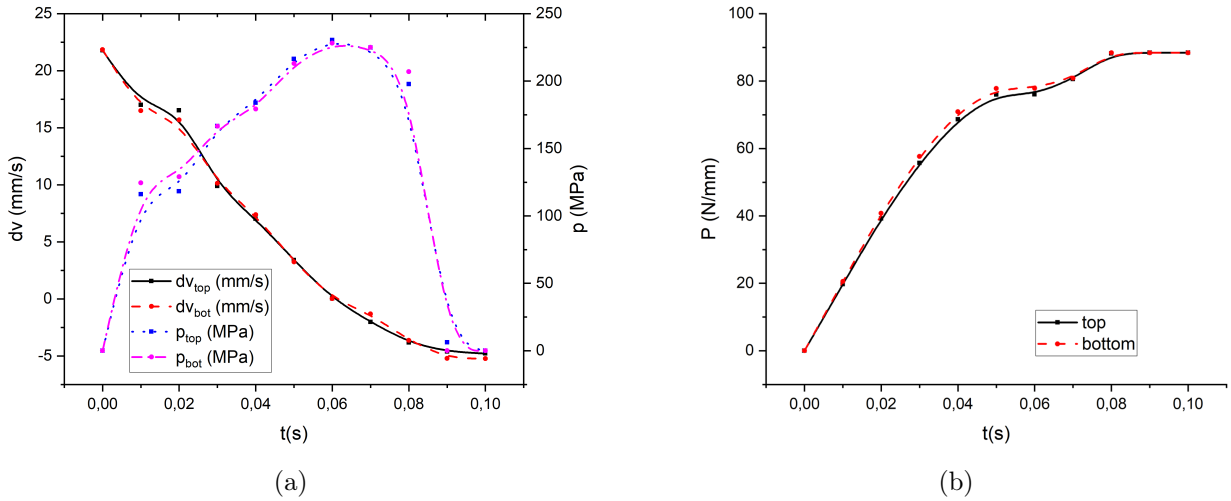

(a) (b)

Figure 2. *a)* Simulation results for symmetric rolling, *b)* Increase in wear value for symmetric rolling

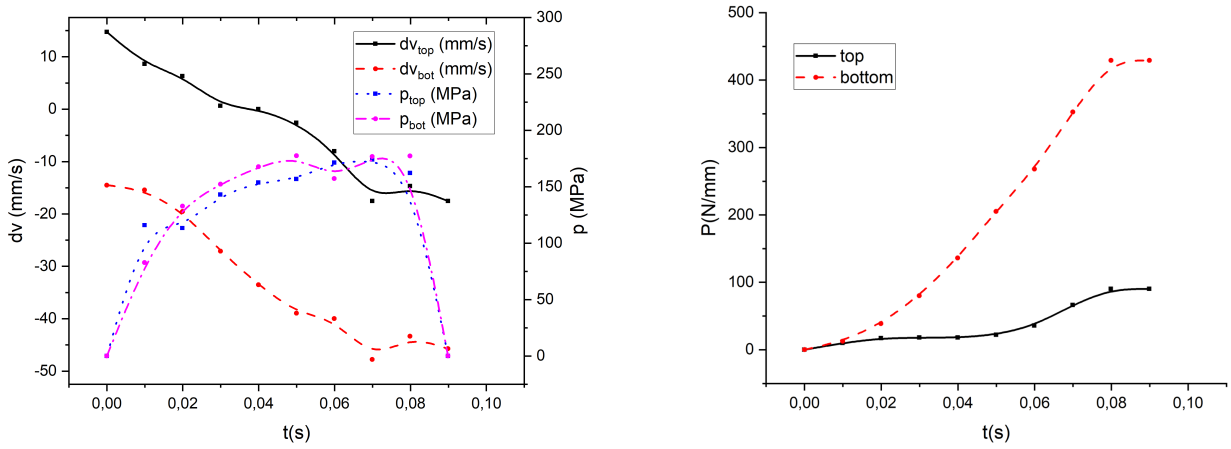

(a) (b)

Figure 3. *a)* Simulation results for asymmetric rolling, *b)* Increase in wear value for asymmetric rolling

due to the different velocity of the rolls. The point of adhesion is formed only in the faster roll. The slower roll develops more wear due to the higher sliding velocity.

3.1. Chagning the friction coefficient

The effect of the friction coefficient was investigated in the range $\mu = 0.075 - 0.25$ for the symmetric and asymmetric cases. The geometric parameters of the test are given in Table 2. In the symmetrical case, the peripheral velocities are the same, in the asymmetrical case, the peripheral velocity of the lower roll is 0.748 rad/s.

Table 2. Parameters used for modelling

Deformation mode	Parameter	Value
SR	ω_t [rad/s]	1.1
ASR	ω_t [rad/s]	1.748
SR+ASR	μ [-]	0.075-0.25

Table 3. Wear in symmetric rolling for different friction coefficients

μ [-]	Δh_t [nm]	Δh_b [nm]
0.075	488.5	505
0.085	530	535
0.1	525	515
0.1125	487	476
0.125	515	520
0.1375	498.5	479
0.15	498.5	510
0.1625	460.5	505
0.175	427	436
0.1875	434	421
0.2	459.5	472
0.2125	515	451.5
0.225	600	535

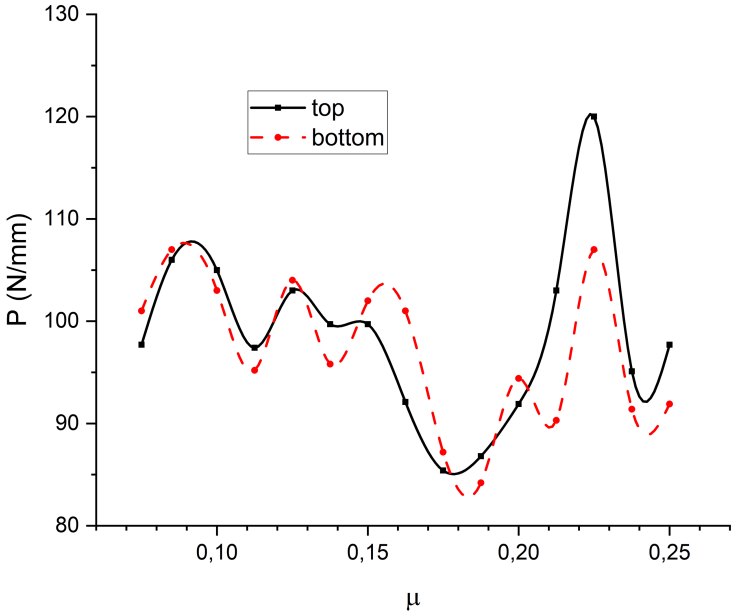

Figure 4. Wear values for symmetrical rolling

For symmetrical rolling, the wear values for different friction factors are given in Table 3 and Fig. 4. For asymmetric rolling the same values are given in Table 4 and Fig. 5.

Table 4. Wear in asymmetric rolling for different friction coefficients

μ [-]	Δh_t [nm]	Δh_b [nm]
0.065	2915	444.5
0.07	2795	458
0.075	2545	398.5
0.1	2470	465.5
0.125	1865	445
0.15	1830	505
0.175	1755	515
0.2	1350	610
0.225	1010	790
0.25	930	750

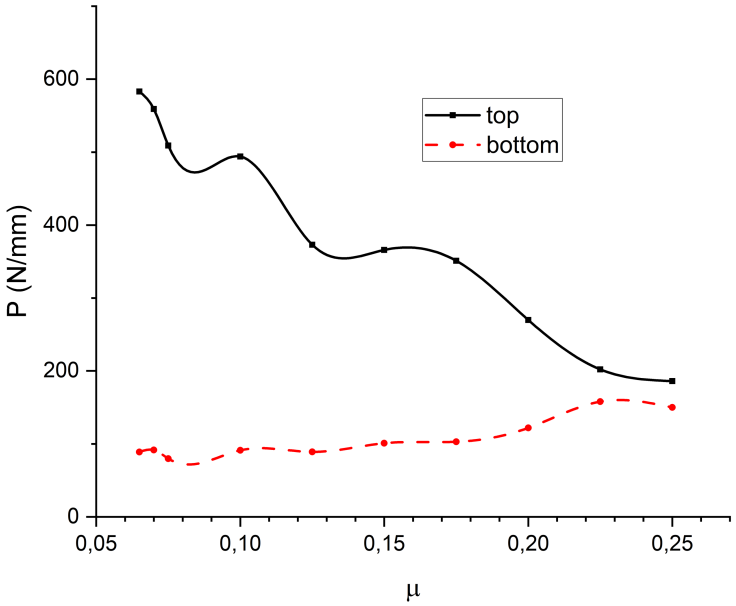

Figure 5. Wear values for asymmetrical rolling

It can be concluded from Table 3 and Fig. 4 that in the case of symmetric rolling, the wear value does not depend on the value of the friction coefficient. In the asymmetric case, as shown in Fig. 5 and Table 4, the wear value for the slower roll does not change significantly and the wear value for the faster roll decreases significantly.

For both rolls in symmetric rolling the following functions can be fitted to the wear values according Eq. (3) and (4).

$$\Delta h_{V\ \max}(\mu, K_V = 1) = k(-12.14\mu + 100.67)\ (R^2 = 0.682) \tag{3}$$

$$\Delta h_{V\ \min}(\mu, K_V = 1) = k(-63.928\mu + 107.4)\ (R^2 = 0.735) \tag{4}$$

For asymmetric rolling the Eq. (5) and (6) can be used.

$$\Delta h_{V\ \max}(\mu, K_V = 1.5) = k(-2091.9\mu + 689.949)\ (R^2 = 0.9652) \tag{5}$$

$$\Delta h_{V\ \min}(\mu, K_V = 1.5) = k(356.02\mu + 55.07)\ (R^2 = 0.821) \tag{6}$$

3.2. Effect of roll velocity ratio

As in the previous study [5], the effect of roll velocity ratio on wear was investigated. The test results are shown in Table 5 and Fig. 6. As shown in Fig. 6 and Table 5, when the velocity ratio is changed, the wear on the slower roll does not change significantly, while the wear on the faster roll increases substantially. The fitted functions for different velocity ratio are the Eq. (7) and (8):

$$\Delta h_{V\ \max}(\mu = 0.15, K_V) = k(481.85K_V - 368.92)\ (R^2 = 0.9485) \tag{7}$$

$$\Delta h_{V\ \min}(\mu = 0.15, K_V) = k(17.141K_V + 62.985)\ (R^2 = 0.821) \tag{8}$$

4. Summary

It has been observed that in symmetric rolling the effect of the friction coefficient on wear is negligible, while in the asymmetric case the wear decreases with increasing the friction coefficient for the rolls with higher velocity. In asymmetrically rolled materials, the wear coefficient does not affect the wear behavior of rolls with lower velocity.

The effect of the velocity ratio was also examined. It has been reported that, with an increase in the velocity ratio; there is a rise in the amount of wear on the faster roll and negligible on the slower one. With further studies, the results can be extended to other geometries and materials. It is important to mention that the analytical functions derived are based on results presented in the current study are of approximative nature and reveal the trend of the wear involved in rolling process.

Table 5. Wear in asymmetric rolling for different K_V values

K_V [-]	Δh_t [nm]	Δh_b [nm]
1.0	442	442
1.05	384.5	515
1.1	412	805
1.25	387	1265
1.5	450.5	2145
1.75	458	2465
2.0	497.5	2700

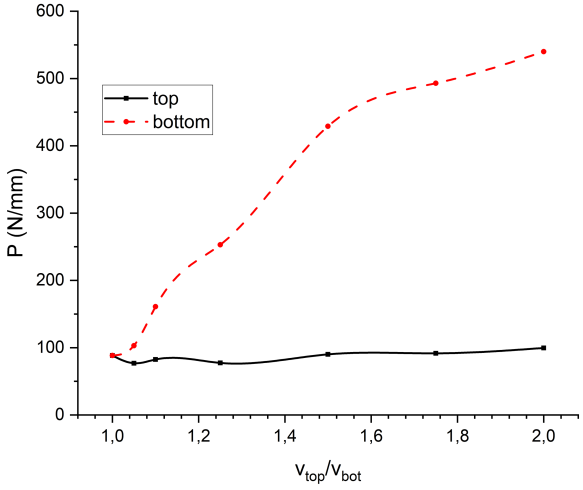

Figure 6. Wear values for different rolling velocities

5. References

[1] Z. Hui, W. Manxing, *A study of wear mechanisms in the cold rolling of aluminium strip*, Journal of Materials Processing Technology 31(1–2), 1992, pp. 235–243. CrossRef

[2] W. da S. Labiapari, C.M. de Alcântara, H.L. Costa, J.D.B. De Mello, *Wear debris generation during cold rolling of stainless steels*, Journal of Materials Processing Technology 223, 2015, pp. 164–170. CrossRef

[3] J. Valíček, M. Harničárová, M. Kušnerová, J. Zavadil, R. Grznárik, *Method of Maintaining the Required Values of Surface Roughness and Prediction of Technological Conditions for Cold Sheet Rolling*, Measurement Science Review 14(3), 2014, pp. 144–151. CrossRef

[4] M. Tahir, *Some aspects on lubrication and roll wear in rolling mills*, Division of Materials Forming Department of Production Engineering Royal Institute of Technology, KTH, Stockholm, 2003, url

[5] A. Pesin, D. Pustovoytov, T. Shveyova, M. Sverdlik, *Finite Element Modeling of Roll Wear during Cold Asymmetric Sheet Rolling of Aluminum Alloy 5083*, MATEC Web of Conferences, 26, 2015, 01010, CrossRef

[6] J.F. Archard, *Contact and Rubbing of Flat Surfaces*, Journal of Applied Physics 24, 1953, p. 981. CrossRef

[7] A. Fischer, K. Bobzin, *Friction, wear and wear protection*, International Symposium on Friction, Wear and Wear Protection 2008, Aachen, Germany, Presented at the International Symposium on Friction, Wear and Wear Protection, Weinheim, Germany: Wiley-VCH. 2009, CrossRef

[8] G. Straffelini, *Friction and Wear*, Cham: Springer International Publishing, 2015, CrossRef

[9] E. Avcu, *The influences of ECAP on the dry sliding wear behaviour of AA7075 aluminium alloy*, Tribology International 110, 2017, pp. 173–184. CrossRef

[10] J. Fluhrer, DEFORM(TM) 2D Version 8.1 User's Manual, Scientific Forming Technolgies Corporation, url

Review: Deformed and recrystallized structures in FCC materials

Purnima Chakravarty[a*], Jurij Sidor[b]

[a] *ELTE, Faculty of Informatics, Savaria Institute of Technology, PhD student*
[b] *ELTE, Faculty of Informatics, Savaria Institute of Technology, full professor*

ABSTRACT

The evolution in the field of recrystallization related studies in FCC metals is summarized in this paper. The process of recrystallization which is initiated by stored energy is provided by dislocations. However, dislocations are introduced during the process of deformation, hence both aspects are covered, as well as the kinetics of recrystallization is well elaborated. The key features of recrystallization: role of misorientations; deformation and recrystallization textures; are described and most importantly recent issues on recrystallization of FCC metals are documented in this paper. The final remarks contain the future aspects of studies in the field of recrystallization of materials with FCC crystal structure.

Keywords: *FCC metals, Recrystallization kinetics, Texture evolution*

1. Introduction

In plastic deformation of metals, dislocations are introduced, and they play a very important role, since the movement of dislocations causes lower deformation energy during the practical forming process of metals compared to one is calculated theoretically for metals without the linear defects [1]. It is possible to explain the mesoscopic changes involved in annealing by means of: nucleation, recovery, recrystallization; that takes place in a metal during the process of annealing in terms of edge dislocations [2].

Annealing is a very important step in the processing route of material. If the material is continuously heated to a high temperature (annealed), thermally activated processes, such as solid-state diffusion, induce mechanisms where the structural defects may be removed or alternatively arranged in configurations of lower energy [3].

Fig. 1 summarizes the major stages of annealing. At the beginning of heat treatment, the point defects are neutralised. The effect of annealing on dislocation is called polygonization as it is presented in Fig. 2. Altogether step-1 to step-3 as described in Fig. 1 is known as recovery [4, 5].

Fig. 2 reveals recovery by polygonization of a bent crystal containing edge dislocations. The phenomenon presented in Fig. 1 clearly shows that at the beginning (Fig. 2/a), the deformed metal has dislocations of both positive and negative Burgers vector. With the rise of temperature (Fig. 2/b) the dislocations of opposite signs (pair) annihilate each other leaving behind linear defects of only one type. In annealing, these excess dislocations will arrange into the low-energy configurations in the form of regular arrays or low angle grain boundaries (LAGBs) as it is shown in Fig. 2/c which

*Corresponding author: Purnima Chakravarty, pc@inf.elte.hu
https://doi.org/10.37775/EIS.2021.2.3

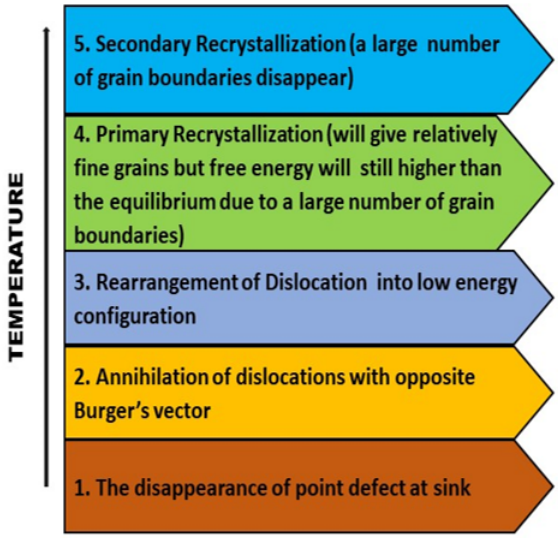

Figure 1. Phenomenon involved in annealing of single-phase metals [3–5]

depicts the phenomenon called polygonization [1, 3]. As shown in Fig. 1, the material shifts towards the process of primary recrystallization (RX) once recovery is over. Recrystallization of the deformed microstructure is known as primary recrystallization to distinguish it from the process of abnormal grain growth which may occur in fully recrystallized material and is sometimes termed as secondary recrystallization, which is revealed by Fig. 3 [3].

It is possible to divide primary RX into two different procedures [3]: (i) Nucleation which corresponds to the first appearance of new grains in the microstructure and (ii) growth during which the new grains replace the deformed structure. The whole process of annealing can be sub-divided into the following steps: a) deformed state, b) Recovery, c) nucleation of new grains, d) partial recrystallization, d) complete recrystallization, e) grain growth and f) abnormal grain growth as shown in Fig. 3.

As metals deformed by the slip mechanism, energy will be accumulated in the material in form of linear defects. During annealing of the material, reduction of the stored energy can take place through relatively slow recovery or by more rapid static recrystallization (SRX). Since recovery proceeds as a continuous process, SRX is a discontinuous process [6].

The process of recrystallization is an extensive transformation phenomenon that is proved to be important in efficient microstructure design. The importance of this process is enhanced due to its capacity to control the structure and properties, specifically structure-sensitive properties of materials [7]. During recrystallization, the deformation in the grain caused by the thermo-mechanical

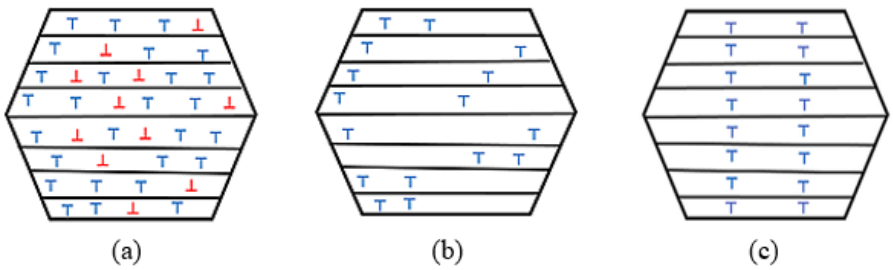

Figure 2. Schematics explaining the phenomenon of polygonization according to [4, 5]: a) Deformed state, b) dislocation annihilation, c) Formation of dislocation walls

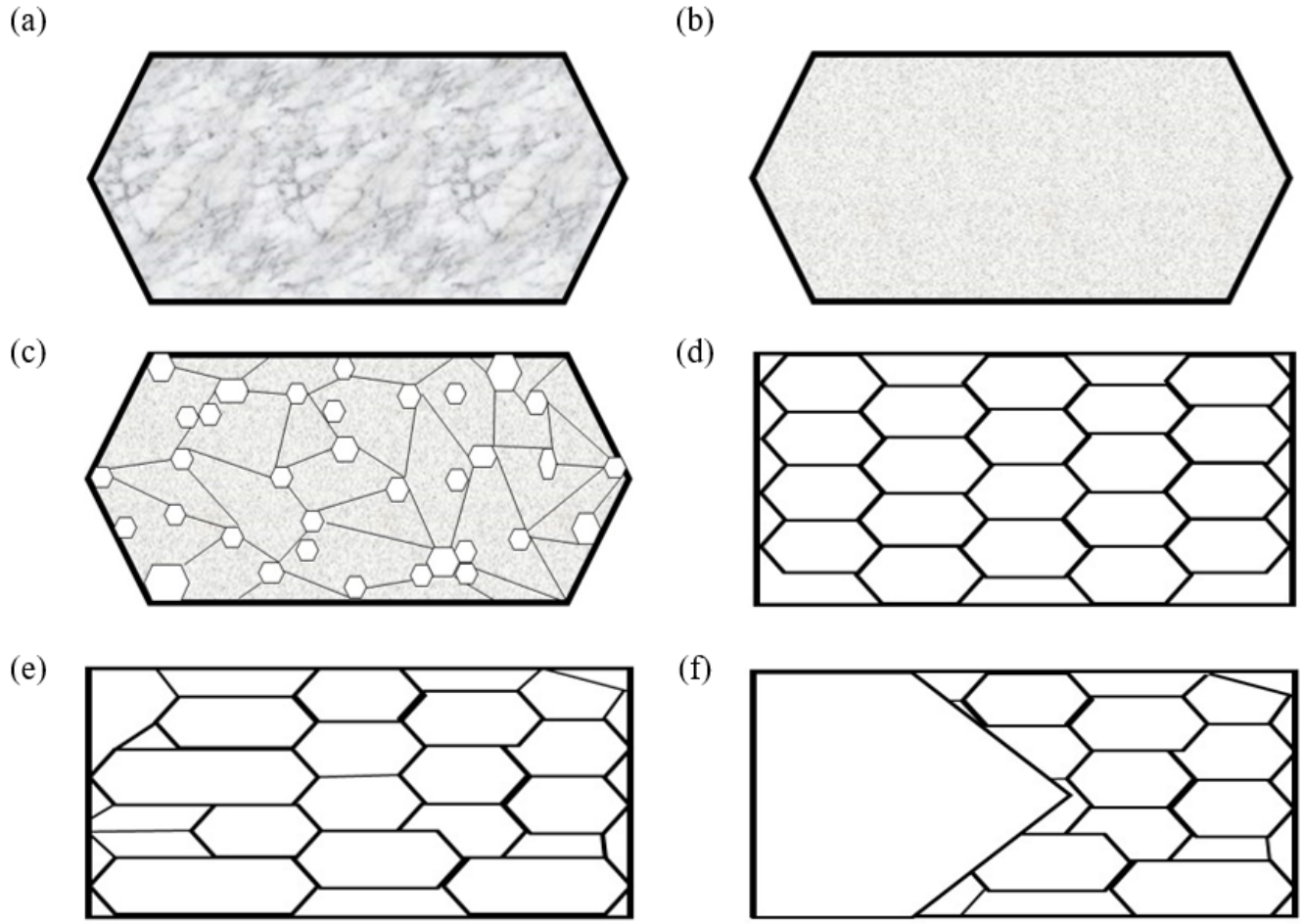

Figure 3. Microstructural changes involved in annealing processes; a) Deformed state, b) Recovered, c) Partially recrystallized, d) Fully recrystallized, e) Grain growth, f) Abnormal grain growth [3]

processing of the material is replaced by new defect-free grains. In short, the recrystallization phenomenon is the corridor towards the development of desirable microstructure as well as the mechanical character of materials [5].

The outcome of annealing process can be seen as the metallurgical changes that return the metal to its pre-cold-worked state. The output of this process results in a reduction of the metal's yield and tensile strength and an increase in its ductility, enabling further cold working. For these changes to occur, the metal must be heated above its recrystallization temperature. However, the recrystallization temperature of a particular metal shows quite a strong composition dependence. The microstructural changes occurring during annealing of a cold-worked metal cause the decrease of stored energy due to plastic deformation. This energy fall is triggered by the mechanisms of rearrangement and annihilation of dislocations (Fig. 2) [7]. It is important to mention that, the factors mentioned above have a direct effect on the recrystallization kinetics.

There is a vast body of experimental evidence and simulation techniques dealing with the structural rearrangements involved in thermomechanical processing of metals. This contribution summarizes the phenomena involved in annealing and analysis the numerical approaches describing the kinetics of recrystallization.

2. The kinetics of recrystallization

The phenomena summarized in Fig. 3 provide a clear picture under the umbrella of the kinetics of recrystallization in terms of Johnson–Mehl Avrami and Kolmogorov (JMAK) equation [8–12]. The qualitative statements on Recrystallization are summarised as laws of Recrystallization, given below [8–14, 16]:

- A certain minimum amount of deformation is mandatory to initiate recrystallization process. The deformation must be sufficient to provide a nucleus to begin recrystallization and to provide the necessary driving force for its growth.
- The temperature at which recrystallization takes place decline as the annealing time increases. The correlation between the recrystallization rate and the temperature is given by the Arrhenius type relation.
- The temperature of recrystallization declines as the strain level is elevated. Causing both nucleation and growth process to take place at a lower temperature in a more highly deformed material.
- The size of recrystallized grain depends mainly on the amount of deformation, which is smaller for heavy deformation. Along with that, the number of nuclei or the nucleation rate is much affected by strain in comparison to the growth rate. Hence, a higher strain will provide more nuclei/unit volume causing smaller final grain size. It has been summarized that, for a respective deformation level the recrystallization temperature will increase with: A larger starting grain size. The grain boundaries are considered to be favoured sites for nucleation. Correspondingly, it is clear that a large initial grain size provides fewer nucleation sites, which causes a drop in nucleation rate. The cumulative effect lead either to a slower recrystallization or the process takes place at higher temperatures.

At higher deformation temperatures, more recovery occurs during the deformation (dynamic recovery), which causes lower stored energy than for a similar strain at a lower deformation temperature. Along with the strain path history of the material, the spatial distribution of orientation or grain orientation of the material must play a major role in controlling the rate of recrystallization. The development of microstructure that can be inferred from the textural rotations has an important bearing on the development of annealing textures in cubic metals [15]. On the other hand, recrystallization of different texture components will occur at different rates and will inevitably lead to inhomogeneous recrystallization [14]. The recrystallization kinetics of both copper and silicon-iron single crystals of various orientations, which had been cold rolled 80%, and significant differences in rates of recrystallization has been observed in [16].

Table 1. Recrystallization of silicon–iron single crystals at 600 °C [16]

Initial orientation	Final orientation	Time for 50% recrystallization [s]	Orientation after recrystallization
{111} <112>	{111} <112>	200	{110} <001>
{110} <001>	{111} <112>	1 000	{110} <001>
{100} <001>	{001} <210>	7 000	{001} <210>
{100} <011>	{100} <011>	No recrystallization	{100} <011>

Brown and Hatherly (1970) [17] investigated the effect of orientation on the recrystallization kinetics of copper single crystals. In this experiment the FCC system had been rolled to a reduction of 98.6% and it has been observed that the recrystallization time at 300 °C varied between 5 and 1000 min [17]. This is compared with a recrystallization time of 1 minute for a polycrystalline specimen deformed to the same strain. Both {110} <112> and {110} <001> crystals developed similar {110} <112> rolling textures, but due to the differences in the nature of the deformed structure, the former recrystallized 50 times slower [3, 17]. Differences between the recrystallization kinetics and textures of the single crystals and the reference polycrystal in the above investigation, serve to highlight the importance of grain boundaries during recrystallization and show that care must be taken in using data from single-crystal experiments to predict the behaviour of polycrystal [3, 18]. Table 1 depicts the variation of recrystallization rate with orientation significantly [16].

The polycrystalline system also reportedly shows differences in the texture formed after hot rolling and annealing lead to differences in recrystallization kinetics when the material is cold rolled and subsequently annealed [19]. The kinetics of recrystallization is classically addressed by the JMAK relation; which shows a sigmoidal time dependence of recrystallization volume fraction [9–12]:

$$X_V = 1 - e^{-Bt^n}. \tag{1}$$

Here the X_V is the fraction of recrystallized grains. The exponent n given by Avrami [12] on the other hand is supposed to depend only on time for the nucleation and growth of recrystallization, temperature independent in nature. In 1979, Sellars [20] reported that the exponent showed independence to temperature and strain rate. If the rates of nucleation and growth remained constant during recrystallization, under such condition n is equal to 4. It is reported by Avrami (1939) [12] that when the rate of nucleation is not constant but rather a decreasing function of time the n varies between 3 and 4, depending on the functional behaviour of nucleation rate.

Under the condition when grains are constrained either by the sample geometry or by some internal microstructural constraint to grow only in one or two-dimensions, then the JMAK exponent are shown in Table 2, which depicts how JMAK exponent varies depending on the growth geometry [3, 7, 12]. Fig. 4 is the pictorial representation of effect of JMAK exponents on recrystallization kinetics. It has been observed, that the depending on the employed JMAK exponent time required for the complete recrystallization varies.

In Eq. (1), term B is defined as:

$$B = \frac{f\dot{N}\dot{G}^3}{4}. \tag{2}$$

Here, f is a shape factor, $4\pi/3$ for the sphere. The two factors nucleation rate $\dot{N}$ and growth rate $\dot{G}$ controls the reaction kinetics [3, 7, 21]. It has been assumed that nuclei are formed at a rate:

$$\dot{N} = \frac{dN}{dt}, \tag{3}$$

where N is nuclei per unit volume during recrystallization. These recrystallization nuclei are the crystallite growing in deformed or recovered material with low internal energy and are separated

Table 2. Ideal JMAK exponents [3, 7, 12]

Growth dimensionality	Site saturation	Constant nucleation rate
3-D	3	4
2-D	1	3
1-D	2	2

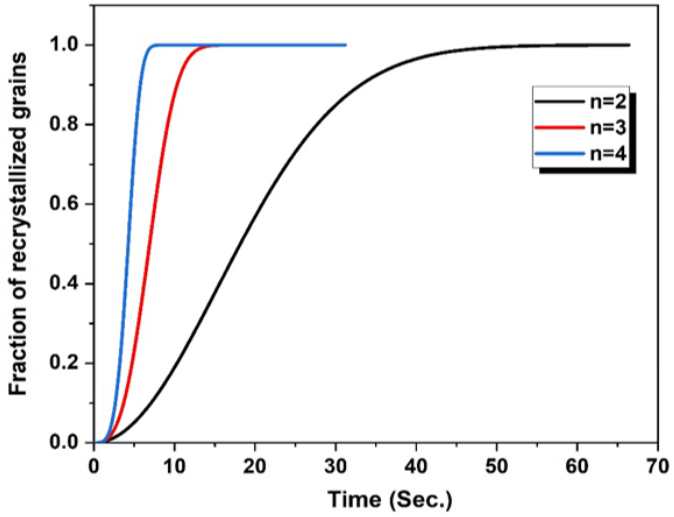

Figure 4. Effect of JMAK exponent on time taken for full recrystallization

by high angle grain boundaries [3, 7, 22]. The growth of new grains is easily detectable during recrystallization. The velocity (v) of a high angle grain boundary, is also defined as the growth rate ($\dot{G}$):

$$v = \dot{G} = MP, \tag{4}$$

where M is the mobility of boundary and P is the net pressure on the boundary. Now, if P_d is the driving pressure for recrystallization, offered by dislocation density ρ that produces stored energy E_d. In this case:

$$P_d = E_d = \alpha\rho Gb^2, \tag{5}$$

where α is constant of the order of 0.5 and b is the Burger's vector [3, 21]. However, the mobility of grain boundaries M is another important quantity is temperature dependent in nature and is usually found to obey an Arrhenius type relationship of the form

$$M = M_o e^{-Q/RT}. \tag{6}$$

The slope of a plot of $\ln(M)$ or $\ln(v)$ (for constant P), against $1/T$, therefore, yields a value of activation energy Q [3]. The mobility of high angle grain boundaries (HAGB) has a significant relation with the process of recrystallization. It has been observed that during recrystallization of cold-deformed materials, isothermal grain boundary migration rates has decrease with time [23]. HAGB shows orientation-dependent characteristics. For example, it been reported by Cook and Richards (1940) [24] and Bowles and Boas (1948) [25] who found rapid growth of certain orientations

Table 3. Orientation dependency of HAGB as well as growth for some FCC metals [3, 27, 29]

Experimentally established results		**Metal**	**Reference**
Rotation [°]	**Axis**		
35-45	<111>	Al	Liebman et al. (1956) [28]
38	<111>	Cu	Kronberg and Wilson (1949) [27]
36-42	<111>	Pb	Aust and Rutter (1959) [29]
23	<100>	Al	May and Erdmann (1959) [3]
19	<100>	Cu	Kronberg and Wilson (1949) [27]

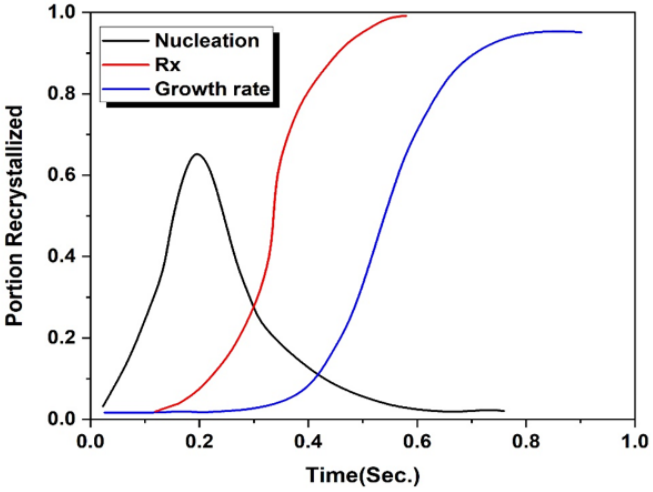

Figure 5. Fraction of recrystallized grains as a function of annealing time for mesoscopic transformations in which temperature is held constant [5, 7, 9–12]

in copper, and Beck et al. (1950) [26] showed that in lightly rolled high purity aluminium, grains with a misorientation of 40° about the <111> axis exhibited the largest growth rate. Along with this, Kronberg and Wilson (1949) [27] who carried out recrystallization experiments on copper, found that grains related to the deformed matrix by a rotation of 22°–38° about a common <111> axis, and by 19° about a <111> axis grew most rapidly. The existence of certain orientation relationships which are associated with a rapid growth rate for some FCC metals has been represented in Table 3.

The cumulative effect of all the parameters in Eq. (1) is pictorial represented in Fig. 5. The time required for nucleation to take place and growth of new grains to begin is known as the incubation period. Fig. 5 shows the kinetics of recrystallization (red line) which is a characteristic sigmoidal curve. The rate of recrystallization increases after the incubation period and shows a linear behaviour before slowing down [3]. On the other hand, nucleation rate (black line) increases with time and achieves maximum, finally decreases, enhancing the process of recrystallization [3, 9–12]. The rate of grain growth (blue line) also increases with time resulting in growth of the recrystallized grains in correlation with Fig. 3. Fig. 5 summarizes the standard behaviour of nucleation, growth and

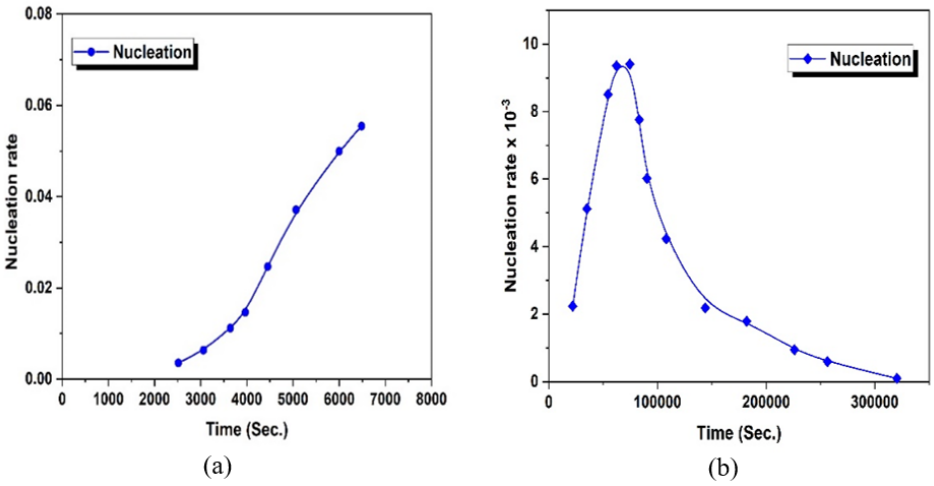

Figure 6. The changes of nucleation rate ($\dot{N}$) with time for aluminium 5% deformed, annealed at 350 °C, a) Initial grain size 45 mm (fine grain), b) initial grain size 130 mm (coarse grain) [14, 30]

recrystallization for the metals annealed at constant temperature and a range of time variation [7]. The nucleation rate itself depends on various factors and the major factor is the size of the initial grain, which can be clearly observed in Fig. 6.

The above two graph shows that depending on initial grain size the nucleation rate shows different behavioural properties. On the other hand, grain growth has various range of dependency factors. The migration of high angle boundaries is the basic mechanism operating during both recrystallization and grain growth [30]. The main difference between them is that the driving force is related to both phenomena. The driving force for grain growth, is the energy of the high angle boundaries, whereas the main driving force for recrystallization is the stored energy, Ed described by Eq. (5). The driving force falls with time during recrystallization, due to simultaneous recovery in the non-recrystallized regions. However, the process of recovery and recrystallization is competitive and is more pronounced in metals and alloys with both body centered cubic (BCC) crystal structure and face centered cubic (FCC) crystal structure with high Staking fault energy (SFE) [7, 14, 30]. Not only the strain heterogeneity but also the occurrence of recovery may lead to a decrease in the speed of grain boundary migration during recrystallization as well as it can slow down the recrystallization process, which can cause possible deviation in the JMAK equation as shown in Fig. 7 [7].

It can be observed from Fig. 7 that, how different level of deformation can have direct effect on the growth rate of the grains as well as on overall process involved in evolution of stress-free grains. Hence, it can be concluded that there are various factors that can affect nucleation and grain growth and thereby recrystallization kinetics.

As well as there are various methodologies in modelling and simulation of recrystallization. Some numerical formulations discussed in this contribution include continuum mechanical models and discrete approaches such as Monte Carlo Potts models and cellular automata as well as vertex, phase field and level set models [31]. However, the statistical models of primary recrystallization are specifically the superposition model and the compromise model, which has been distinguished by Bunge Kohl (1996) [32]. Both models can describe oriented nucleation, orientation dependence

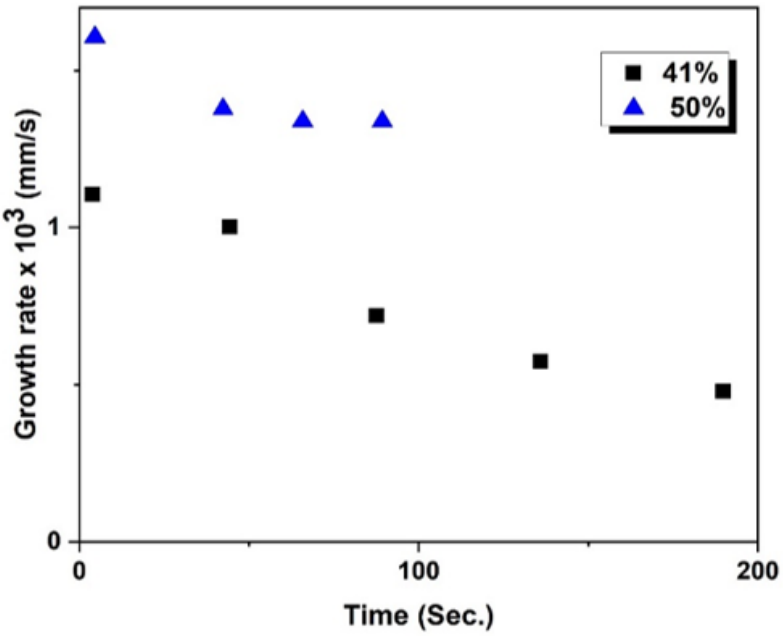

Figure 7. Variation in growth rate in AA3000 Aluminum alloy annealed at 400 °C with 41% and deform 50% deformation [7]

of driving force, and misorientation dependence of boundary mobility. The superposition model demands abundant nucleation, whereas the compromise model corresponds to sparse nucleation. On the other hand, it has been observed that the statistical compromise model is able to explain the most prominent texture types in cubic metals (both FCC & BCC) [32].

3. The importance of recrystallization and deformed texture

The grain orientations in polycrystal, are distributed with a certain preferred orientation. It has been observed that, most of the materials exhibit with some exact pattern in the orientations. Along with that there exists a tendency for the occurrence of particular orientations during crystallization from a melt and as well as by consecutive thermomechanical processes. This tendency is known as preferred orientation or, more precisely, texture. The importance of texture to materials holds in the fact that, many material properties are texture specific [33]. In a similar manner, during the process of recrystallization new texture evolves in the material which is different from the texture of deformed state; these new textures reflect thermo- mechanical processing history of the work piece.

FCC metals like Cu, Au, Ag, Al are usually soft and ductile, which indicates that they can be bent and shaped easily. On the other hand, these metals show comparatively lower strength. The deformation textures of FCC metals are basically characterised by the stacking fault energy (SFE). For high SFE metals like aluminium the corresponding textures are known as pure metal or copper type rolling texture to separate it from textures evolved in low SFE value FCC metals. The influence of SFE on texture evolution is explained in terms of mechanism involved in the process of deformation. In case of metals with high to medium stacking fault energy the process of deformation is primarily dominated by slip of dislocations [3, 33, 34]. The fundamental pure metal textures are given by the Brass orientation {011} <112>, the Copper orientation {112} <111> and the S orientation {123} <634> [34, 35]. However, for the crystallographic models with twinning as well as for conventional models there are two types of rolling texture obtained; namely brass-type texture and the copper-type texture which are experimentally observed as well [44]. Table 4 shows texture components and fibers, which typically evolve in FCC metals during deformation.

Table 4. Texture components in rolled FCC metals [3]

Texture Component, symbol	{hkl}	<uvw>	Φ_1 [°]	Φ_2 [°]	Φ_3 [°]
Copper, C	112	111	90	35	45
S	123	634	59	37	63
Goss, G	011	100	0	45	90
Brass, B	011	211	35	45	90
Dillamore, D	4,4,11	11,11,8	90	27	45
Cube	001	100	0	0	0

Table 5. Fibers in rolled FCC metals [3, 33]

Fibre	**Common axis of orientation**
α	<011>//ND
β	$\{h,1,h+1\} < \frac{h(h+1)}{3/4-h}, \frac{2h(h+1)}{1/2-h}, \frac{h^2}{h-3/4} + \frac{2h}{h-1/2} >$
Γ	<111>//ND
θ	<001>//ND
η	<001>//RD

The fiber as shown in Table 4 and 5 is a group of orientation with a common plane parallel to the particular macroscopic axis. Due to crystal symmetry, it is possible that one fiber may appear several times in the Euler space [33].

The range of recrystallization textures seen in FCC metals and alloys is much wider and more complex than is the case of the corresponding deformation textures, and under many conditions, the origin of the textures is still a matter of discussion. The formation of recrystallization texture is characterised not only by the formation as well as movement of high angle grain boundaries, which is accomplished by the process of nucleation and grain growth [3, 33, 34]. Along with that, there are various other factors that may affect the recrystallization texture in FCC metals. For example, we can discuss the effects of prior grain size, rolling reduction and annealing temperature. In case of 70:30 brass after annealing for 1 hour at 300 °C (low temperature) the texture of material cold rolled with 92% reduction changed from the normal {236} <385> to {110} <110> as the prior grain size increased, but the magnitude of the change was strain dependent and non-existent at 97% reduction. Annealing at high temperatures (600 °C) led to a {113} <332> texture for small grain sized material and high reductions. After low reductions the {110} and more general {110} orientations. The {110} <112> texture was present to higher strain levels as the grain size increased. It seems to be a probable case, that at high temperature {113} <332> texture involved grain growth, and in the 97% rolled material, on the other hand when grain growth was limited by the specimen thickness and the short annealing times, the texture was {236} <385>. For all grain sizes investigated (30-3000 μm) the texture of heavily rolled material was {236} <385> after annealing at 300 °C, and {113} <332> for 600 °C annealing. These results illustrate the importance of grain growth effects on annealing textures [3]. However, considering the fact of orientation growth it has been reported by Liebmann that the growth of new grains during recrystallization is preferred in a particular orientation with respect to the deformed matrix [28]. For pure aluminium the preferred orientation and highest mobility is observed when, grain boundaries rotate with a relationship of approximately 40° about a <111> axis [36]. Taking account of all the effecting factors discussed above most common recrystallization texture in FCC system are listed below.

At the same time, it is one of the most striking features of recrystallization that the texture produced by heavy deformation can be completely modified by recrystallization. There are at least three different types of recrystallization texture known to be produced by recrystallization: a) at

Table 6. Texture components in rolled FCC metals [3]

Texture Component and Miller indices	{hkl}	<uvw>	Φ_1 [°]	Φ_2 [°]	Φ_3 [°]
Cube	001	100	0	0	0
Cube_{RD}	013	100	0	22	0
Cube_{ND}	001	310	22	0	0
Cube-twin (first generation)	122	212	27	48	27
Goss	011	100	0	45	0
BR	236	385	80	31	35
U (transition)	285	121	45	35	20
R	124	211	53	36	60
P	011	122	65	45	0
Q	013	231	45	15	10

one extreme the deformation texture components can be essentially retained, b) in other cases the texture can be strongly randomized and, finally, c) a component that is only a negligible fraction of the deformation can become an overwhelmingly dominant feature of the recrystallization texture. It has been observed that heavily cold rolled commercial pure Aluminium, containing a high density of iron-rich constituents, can give a significant deformation texture while high-purity Aluminium can give rise to a very strong new orientation, that of the cube {001} <100> [37].

4. Recent issues on recrystallization of FCC metals

From 1881, when Kalischer first acknowledged the phenomenon of recrystallization to the current time a lot of progress has taken place in the field of studies of recrystallization [38]. This section is focused on recent revelations done in the field of recrystallization of FCC metals. It is focused mostly on thermomechanical treatment and microstructure control for the metals in interest.

It has been observed that high purity aluminium (>99.99% Al), copper (99.995% Cu), and nickel (99.988% Ni) shows dominant recrystallization cube texture under the following conditions [39]:

- A cube substructure must be present in the deformed matrix of the heavily rolled material.
- This cube texture must play the role of recrystallization nuclei.
- This cube nuclei should grow rapidly by means of migration of high angle boundaries.
- It is possible for the cube grains to grow at the expense of the other small grains because of the size effect, which makes the cube texture dominant and unique at the same time.

It has been observed that the strong cube texture can be obtained after the primary recrystallization under the above conditions, but the size of cube grains can also be larger than those of other grains. In this case, it is considered that the cube texture is strengthened by grain growth during further annealing and becomes a dominant final texture with the help of surface effect. Along with that, it is possible that some substructure with cube orientation has certain stability during the process of rolling and can remain in the deformed matrix after heavy rolling. This shows higher preference for the cube component in becoming recrystallization nuclei and growing in comparison to other substructures. All these characteristics of cube texture are closely related to the condition of crystallographic geometry in rolling deformation and lead to a final dominant cube texture [39].

The cube orientations are a finite, but very small component of the usual FCC rolling texture. On recrystallization after suitable deformation, the minor cube component of the deformation texture in some cases becomes the dominant part of the recrystallization texture. There are some observations done about the dominating cube component, given as [3, 40]:

- The increase in cube texture is initiated by the enhancing the quantity of cube grains, as well as by the decrease in their divergence from the perfect cube orientation.
- The cube grains tend to nucleate through deformation bands along the rolling direction.
- On average, each cube grain tends to split into seven misoriented bands throughout the process of plane-strain compression. On the other hand, these grains tend to break into three misoriented bands during plane-strain extrusion.
- Each grain with primary cube structure tends to give rise to at least one deformed cube band while deformed. Which causes the spacing between cube structures to decrease in a predictable manner with strain.
- The cube grains obtained in final texture enhances greatly in strength as prior strain was increased [40].

It has been documented that the β-fibre can be exactly described in the first, second and third Euler subspaces by the analytical expression given below [41]:

$$\{h, 1, h+1\} < \frac{h(h+1)}{3/4-h}, \frac{2h(h+1)}{1/2-h}, \frac{h^2}{h-3/4} + \frac{2h}{h-1/2} >, \tag{7}$$

that describes the rolling texture in both pure metals and alloys of medium and high SFE with FCC structure in spite of the varieties in the chemical composition and thermo-mechanical processing parameters [41]. At the same time, asymmetric rolling of FCC metals like Al tend to provide a finer recrystallized grain structure as compared to conventionally produced material. According to Sidor and Kestens for High SFE FCC metals like Al the larger amount of accumulated strain leads to an increased population of nuclei, which causes fine-grained structures [42].

It has been observed that strain mode applied in both hot and cold rolling processes significantly affects the final recrystallization texture when experiment has been conducted on Aluminium alloy of 6xxx series. The recrystallization textures produced in the Asymmetric Rolling process improve the normal anisotropy, whereas the in-plane anisotropy does not benefit momentously from the Asymmetric rolling process. Results of crystal plasticity calculations show that an improved normal anisotropy in asymmetrically rolled sheets ensures an increased limiting drawing ratio, which is in favour of enhanced formability [43].

5. Conclusions

Formation of recrystallization texture, in general, and FCC cube recrystallization texture, specifically, is of considerable scientific and industrial interest. As the substitution of steel with light metals is an effective way to reduce the weight of car bodies. FCC metals like Aluminium alloys are an attractive candidate for automotive applications because of their favourable strength-to-weight ratio and high corrosion resistance characteristic. However, the soft and ductile nature of FCC metals makes it difficult to process during specific forming procedures.

It can be concluded that a large volume of scientific and technological knowledge has been accumulated in the field of study. Although various scientific aspects still need further attention. Research till the date in the field of analysis of recrystallization texture avails us with the knowledge of control over the microstructure of metallic materials during its thermomechanical processing. Hence, using the idea of texture control in various FCC mechanical properties of the respective metals can be improved.

6. References

[1] E. Orowan, *To crystal plasticity II*, Magazine for Physics 89, 1934, pp. 614-633. CrossRef

[2] F.J. Humphreys, *Nucleation in Recrystallization*, Materials Science Forum 467-470, 2004, pp. 107-116. CrossRef

[3] F.J. Humphreys, G.S. Rohrer, A. Rollett, *Recrystallization and Related Annealing Phenomena, Third edition*, Elsevier: Amsterdam, The Netherlands, 2017.

[4] R.D. Doherty, D.A. Hughes, F.J. Humphreys, J.J. Jonas, D. Juul Jensen, M.E. Kassner, W.E. King, T.R. McNelley, H.J. McQueen, A.D. Rollett, *Current issues in recrystallization:a review*, Materials Science and Engineering 238, 1997, pp. 219-274. CrossRef

[5] W.D. Callister, D.G. Rethwisch, *Materials Science and Engineering: An Introduction, Seventh Edition*, John Wiley & Sons, New York, 2007.

[6] K. Huang, R.E. Logé, *A review of dynamic recrystallization phenomena in metallic materials*, Materials & Design 111, 2016, pp. 548-574. CrossRef

[7] P.R. Rios, F.S. Jr; H.R.Z. Sandim, R.L. Plaut, A.F. Padilha, *Nucleation and growth during recrystallization*, Materials Research 8, 2005, pp. 225-238. CrossRef

[8] A.N. Kolmogorov, *On the Statistical Theory of Crystallization of Metals*, Bulletin of the Academy of Sciences of the USSR Ser. Math 3, 1937, pp. 355-359. CrossRef

[9] W.A. Johnson, R.F. Mehl, *Reaction kinetics in processes of nucleation and growth*, Transactions of the American Institute of Mining and Metallurgical Engineers 135, 1939, pp. 416-442.

[10] M. Avrami, *Granulation, Phase Change and Microstructure Kinetics of Phase Change III*, The Journal of Chemical Physics 9, 1941, pp. 177-184. CrossRef

[11] M. Avrami, *Kinetics of Phase Change II, Transformation-Time Relations for Random Distribution of Nuclei*, The Journal of Chemical Physics 8, 1940, pp. 212-224. CrossRef

[12] M. Avrami, Kinetics of Phase Change I, General Theory, The Journal of Chemical Physics 7, 1939, 1103-1112. CrossRef

[13] R.F. Mehl, *ASM Metals Handbook*, ASM, Metals Park, Ohio, 1948.

[14] J.E. Burke, D. Turnbull, *Recrystallization and grain growth*, Progress in Metal Physics 3, 1952, pp. 220-292. CrossRef

[15] I.L. Dillamore, H. Katoh, *The Mechanisms of Recrystallization in Cubic Metals with Particular Reference to Their Orientation-Dependence*, Material Science 8, 1974, pp.73-83. CrossRef

[16] W.R. Hibbard, W.R. Tully, *The effect of orientation on the recrystallization kinetics of cold-rolled single crystals*, AIME TRANS 221, 1961, pp. 336-343.

[17] K. Brown, M. Hatherly, *Rolling and recrystallization textures of copper single crystals*, Journal of the Institute of Metals 98, 1970, pp. 310-317.

[18] K. Brown, M. Hatherly, *Recrystallization kinetics of rolled copper single crystals*, Journal of the Institute of Metals 98, 1970, pp. 317-320.

[19] J.C. Blade, A.J. Bryant, A.T. Thomas, *Alloy composition and microstructure control in relation to mechanical working for aluminium alloys*, Metals Technology 3, 1976, pp. 380-386. CrossRef

[20] D.R. Barraclough, C.M. Sellars, *Static recrystallization and restoration after hot deformation of type 304 stainless steel*, Metal Science 13,1979, pp. 257-268. CrossRef

[21] J.W. Christian, *The Theory of Transformations in Metals and Alloys, First edition*, Pergamon, Oxford, 2002. CrossRef

[22] P. Cizek, F. Bai, E.J. Palmiere, W. M. Rainforth, *EBSD study of the orientation dependence of substructure characteristics in a model Fe-30wt% Ni alloy subjected to hot deformation*, Journal of Microscopy 217, 2005, pp. 138-151. CrossRef

[23] R.A. Vandermeer, D.J. Jensen, *The Migration of High Angle Grain Boundaries during Recrystallization*, Interface Science 6, 1998, pp. 95–104. CrossRef

[24] M. Cook, T.L. Richards, *The Structural Changes in Copper Effected by Cold Rolling and Annealing*, Journal of the Institute of Metals 66, 1940.

[25] J.S. Bowles, and W. Boas, *The effect of crystal arrangement on secondary recrystallization in metals*, Journal of the Institute of Metals 74, 1948, pp. 501-519.

[26] P.A. Beck, P.R. Sperry, H. Hu, *The orientation dependence of the rate of boundary migration*, Journal of Applied Physics 21, 1950, pp. 420-425. CrossRef

[27] M.L. Kronberg, F.H. Wilson, *Secondary recrystallization in copper*, Transactions of the Metallurgical Society of AIME 185, 1949, pp. 501-514.

[28] B. Liebman, K. Lücke, G. Masing, *Untersuchung über die Orientierungsabhängigkeit der Wachstumsgeschwindigkeit bei der primären Rekristallisation von Aluminium-Einkristallen*, International Journal of Materials Research 47, 1956, pp. 57-63. CrossRef

[29] K.T. Aust, J.W. Rutter, *Grain boundary migration in high-purity lead and dilute lead-tin alloys*, Transactions of the Metallurgical Society of AIME 215,1959, pp. 119-127.

[30] W.A. Anderson, R.F. Mehl, *Recrystallization of aluminum in terms of the rate of nucleation and the rate of growth*, Trans. AIME 161, 1945.

[31] H. Hallberg, *Approaches to Modeling of Recrystallization*, Metals 1, 2011, pp. 16-48. CrossRef

[32] H.J. Bunge, U. Kohler, *Modelling Primary Recrystallization in fcc and bcc Metals by Oriented Nucleation and Growth With the Statistical Compromise Model*, Texture, Stress, and Microstructure 28, 1997, pp. 231-259. CrossRef

[33] O. Engler, V. Randle, *Introduction to texture analysis: macrotexture, microtexture and orientation mapping, Second Edition*, CRC Press/ Taylor & Francis, Boca Raton, 2009. CrossRef

[34] O. Engler, K. Lacke, *Mechanisms of recrystallization texture formation in aluminium alloys*, Scripta Metallurgica et Materialia 27, 1992, pp. 1527-1532. CrossRef

[35] J. Hirsch, K. Lücke, *Mechanism of deformation and development of rolling textures in polycrystalline fcc metals — I. Description of rolling texture development in homogeneous CuZn alloys*, Acta Metallurgica 36, 1988, pp. 2863-2882. CrossRef

[36] D.A. Molodov, U. Czubayko, G. Gottstein, L.S. Shvindlerman, *Mobility of <111> tilt grain boundaries in the vicinity of the special misorientation $\sum$=7 in bicrystals of pure aluminium*, Scripta Metallurgica et Materialia 32, 1995, pp. 529-534. CrossRef

[37] R.D. Doherty, *Recrystallization and texture*, Progress in Materials Science 42, 1997, pp. 39-58. CrossRef

[38] S. Kalischer, *Ueber die Molekularstruktur der Metalle*, Berichte der deutschen chemischen Gesellschaft 15, 1882, pp. 702-712. CrossRef

[39] W. Mao, *Formation of Recrystallization Cube Texture in High Purity Face-Centered Cubic Metal Sheets*, Journal of Materials Engineering and Performance 8, 1999, pp. 556-560. CrossRef

[40] I. Samajdar, R.D. Doherty, *Cube recrystallization texture in warm deformed aluminum: understanding and prediction*, Acta Materialia 46, 1998, pp. 3145-3158. CrossRef

[41] J.J. Sidor, L.A.I. Kestens, *Analytical description of rolling textures in face-centred-cubic metals*, Scripta Materialia 68, 2013, pp. 273-276. CrossRef

[42] J. Sidor, R.H. Petrova, L.A.I. Kestens, *Deformation, recrystallization and plastic anisotropy of asymmetrically rolled aluminum sheets*, Materials Science and Engineering: A 528, 2010, pp. 413-424. CrossRef

[43] J.J. Sidor, R.H. Petrov, L.A.I. Kestens, *Texture-Induced Anisotropy in Asymmetrically Rolled Aluminium Alloys*, Advanced Engineering Materials 13, 2011, pp. 949-954. CrossRef

[44] U.F. Kocks, C.N. Tomé, H-R. Wenk, Texture and Anisotropy, First edition, Cambridge University Press, Cambridge, 1998.

Wear analysis of natural-inorganic fiber reinforced brake composites using Taguchi's technique

Tej Singh[a*], Gusztáv Fekete[a]

[a] *ELTE, Faculty of Informatics, Savaria Institute of Technology, associate professor*

ABSTRACT

Brake friction composite materials comprising varying proportions of natural (banana) and inorganic (lapinus) fibers were designed, fabricated by compression moulding and characterized for sliding wear performance. The sliding wear properties of the manufactured friction composites have been studied by the Taguchi method. An orthogonal array (L_{16}) was used to investigate the influence of sliding wear parameters. A series of tests were conducted on a pin-on-disc machine by considering four control parameters: composition, normal load, sliding velocity, and sliding distance, each having four levels. The results showed that the wear in terms of weight loss decreases with increasing banana fiber and increases with increasing lapinus fiber, normal load, sliding velocity and sliding distance. The results indicate that the normal load emerges as the most significant control parameter affecting wear performance, followed by sliding distance and sliding velocity.

Keywords: *Sliding wear, Friction composite, Natural fiber, Taguchi*

1. Introduction

Composite friction materials are widely used for automotive braking applications. Friction composites contain more than twenty components (classified as space fillers, binders, reinforcing fibers and friction modifiers), which work together to produce a high and stable friction coefficient and low wear over a wide range of operating conditions [1, 2]. Literature related to the role of various reinforcing fibers, space fillers, binders, property modifiers and nanofillers is widely reported [3–7]. Similarly, optimization of friction materials using decision-making models and several soft computing-based techniques are reported to optimize friction composites [8]. Among various components, fibrous reinforcements: such as organic fibers, inorganic fibers, metallic fibers, and their combinations, have been found to play an important role as they reinforce composites during production and also help in the formation of topographical features which help in the increment of tribological properties [9]. These fibers are synthetic and display many drawbacks, including non-recyclability, higher cost and energy consumption. Moreover, the wear particles generated during the braking also contain several hazardous elements that threaten the environment. In addition, the wear particles released during braking reported containing a few hazardous components which previously demonstrated danger to the environment [10]. Nowadays, natural fibers are extensively used in many applications and can be proved a potential candidate for friction composites because of various beneficial characteristics, including biodegradability [11–14]. Lapinus fiber is an inorganic mineral and contains a significant quantity of silica, alumina, calcium oxide, and magnesium oxide [15]. Lapinus fiber has high thermal

*Corresponding author: Tej Singh, sht@inf.elte.hu
https://doi.org/10.37775/EIS.2021.2.4

Table 1. Ingredients and designation

Composition [wt.%]	Composite designation			
	BL-1	BL-2	BL-3	BL-4
Base composition*	70	70	70	70
Banana fiber	2.5	5	7.5	10
Lapinus fiber	27.5	25	22.5	20

* Graphite=5 wt.%, Barium sulphate=50 wt.%, Phenolic resin=15 wt.%

stability and has improved the tribological characteristics of brake friction materials under a wide range of operating conditions [15, 16]. Therefore, the effect of natural fiber in combination with inorganic fiber on wear performance of brake friction composite was assessed and reported in this article.

2. Experimental details

2.1. Materials and fabrication

The friction composites used in the present study consists of phenolic resin, banana fiber, lapinus fiber, barium sulphate and graphite amounting to 100% by weight were fabricated. Detailed descriptions for each manufacturing condition are briefly reported elsewhere [11, 12]. Specimen of size 20 mm x 10 mm x 10 mm were cut from the fabricated friction composites for this research work.

2.2. Sliding wear test

The wear performance of the manufactured friction composites was studied using a pin-on-disc machine (DUCOM) as per ASTM G 99 [17]. A series of tests are conducted with selected operating conditions of load, velocity and distance. The material loss from the composite surface before, and after testing was measured and the wear in terms of weight loss (Δw) was reported using Eq. (1):

$$\Delta w = w_i - w_f, \tag{1}$$

where w_i and w_f were the sample weight before after testing.

2.3. Taguchi based experimental design

The experimental design was created in order to see how introducing control elements affected the method's outcomes. Taguchi is a method for designing experiments to obtain data in a controlled mode while optimizing the task using certain variables. It is a straightforward and methodical strategy of optimizing design for quality, cost, and performance and is widely utilized in industrial, management, and research applications [18–20]. This procedure entails a series of tests to determine the appropriate parameters for low wear and friction characteristics. The output is estimated for all collections of the evaluated levels of a factor in the Taguchi technique. This method can be used to investigate input variables by determining the significant components that influence the outcome. In addition, the investigation may offer the best set of these factors [18]. The method used orthogonal array design to reduce the number of experiments [19]. In this study, the L16 orthogonal array was constructed using the Taguchi technique to study the influence of selected operating parameters on the wear performance of the manufactured friction composites. Minitab® 17 was used to create a mathematical model and find the best conditions for minimizing sliding wear. There were 16 experimental runs with four control factors at four levels. The sliding wear tests on the composites

Table 2. Control parameters and levels used in the experiment

Control parameters	Levels			
	I	II	III	IV
A: Composition [wt.%]	BL-1	BL-2	BL-3	BL-4
B: Normal load [N]	25	50	75	100
C: Sliding velocity [m/s]	1.5	3	4.5	6
D: Sliding distance [m]	1 000	2 000	3 000	4 000

are carried out under different operating conditions considering four control parameters, composition, sliding velocity, normal load and sliding distance each at four levels as listed in Table 2. After that, signal-to-noise ratio (SNR) analysis of the obtained experimental results was carried out to determine the optimal combination of control parameters resulting in lower wear. There are three types, namely higher-the-better, lower-the-better and nominal-the-better, applicable for SNR analysis. In the study of friction composites, one of the most important targets is identifying the combination of control parameters under which minimum wear would occur. Therefore, lower-the-better analysis was used in this study and SNR was calculated using Eq. (2) [18–20].

$$SNR = -10\log\frac{1}{\alpha}\sum\beta^2, \tag{2}$$

where α is number of tests, and β is the weight loss. Following SNR analysis, the effictiveness of each control parameter on wear performance was evaluated in terms of contribution ratio using using following steps [20]:

Step #1: The overall SNR mean ($\overline{SNR}$) is computed as:

$$\overline{SNR} = \frac{1}{16}\sum_{\alpha=1}^{16}(SNR). \tag{3}$$

Step #2: In this step level mean of SNR (ω) for each control parameter was computed as:

$$\omega_i = \frac{1}{4}\sum_{j=1}^{4}(SNR)_{ij}, \tag{4}$$

where i is the control parameter and j means the corresponding level.

Step #3: In this step sum of square value ($\overline{\omega}$) for each control parameter was determine using variations of ω_i with respect to $\overline{SNR}$ as:

$$\overline{\omega_i} = \sum_{J=1}^{5}(\omega_i - \overline{SNR})^2. \tag{5}$$

For all control parameter it can be determined as:

$$\overline{\omega} = \sum_{i=1}^{4}(\omega_i - \overline{SNR})^2. \tag{6}$$

Step #4: Finally the contribution ratio (Δ_i) for each control parameter was determine using following equation:

$$\Delta_i = \frac{\overline{\omega_i}}{\overline{\omega}}100. \tag{7}$$

The overall mean ($\overline{SNR}$) for the conducted 16 experiments was determined using Eq. (3) and found to be 43.68 dB. The level mean of SNR (ω) values for each control parameter are computed by using Eq. (4). For composition, the ω value determined as:

$$\omega(\text{composition, BL-1}) = \frac{1}{4}[51.70 + 42.82 + 32.43 + 26.86] = 38.45, \tag{8}$$

$$\omega(\text{composition, BL-2}) = \frac{1}{4}[49.44 + 48.60 + 50.12 + 32.63] = 45.20, \tag{9}$$

$$\omega(\text{composition, BL-3}) = \frac{1}{4}[44.72 + 37.10 + 49.05 + 45.45] = 44.08, \tag{10}$$

$$\omega(\text{composition, BL-1}) = \frac{1}{4}[47.89 + 51.90 + 47.68 + 40.54] = 47.00. \tag{11}$$

Similarly for sliding distance value computed as:

$$\omega(\text{sliding distance, 1 000 m}) = \frac{1}{4}[51.70 + 50.12 + 45.45 + 51.90] = 49.79, \tag{12}$$

$$\omega(\text{sliding distance, 2 000 m}) = \frac{1}{4}[42.82 + 32.63 + 49.05 + 47.89] = 43.10, \tag{13}$$

$$\omega(\text{sliding distance, 3 000 m}) = \frac{1}{4}[32.43 + 49.44 + 37.10 + 40.54] = 39.88, \tag{14}$$

$$\omega(\text{sliding distance, 4 000 m}) = \frac{1}{4}[26.86 + 48.60 + 44.72 + 47.68] = 41.97. \tag{15}$$

For individual control parameter the value determined using Eq. (5) as follows:

$$\overline{\omega}_{\text{composition}} = [(38.45 - 43.68)^2 + (45.20 - 43.68)^2 + (44.08 - 43.68)^2 + (47.00 - 43.68)^2] = 40.85. \tag{16}$$

Similarly for sliding distance it can be determined as:

$$\overline{\omega}_{\text{sl.dist.}} = [(49.79 - 43.68)^2 + (43.10 - 43.68)^2 + (39.88 - 43.68)^2 + (41 - 97 - 43 - 68)^2] = 55.03. \tag{17}$$

For all control parameters $\overline{\omega}_i$ value can be determined using Eq. (6) as:

$$\overline{\omega} = [\overline{\omega}_{\text{composition}} + \overline{\omega}_{\text{normal load}} + \overline{\omega}_{\text{sliding velocity}} + \overline{\omega}_{\text{sliding distance}}], \tag{18}$$

$$\overline{\omega} = [40.85 + 79.44 + 42.37 + 55.03] = 217.69. \tag{19}$$

Finally the Δ_i value for contribution ratio of each control parameter was computed using Eq. (7) as:

$$\Delta(\text{composition}) = \frac{40.85}{217.69} \cdot 100 = 18.77\%. \tag{20}$$

Similarly for sliding distance Δ_i value computed as:

$$\Delta(\text{sliding distance}) = \frac{55 - 03}{217.69} \cdot 100 = 25.28\%. \tag{21}$$

The mean of means value was the average wear value for each level of each control parameter. For example, in Table 3, the mean of means value for level I (BL-1) of control parameter A is obtained

Table 3. Experimental design and wear results with corresponding SNR

Test run	A	B	C	D	Wear [g]	SNR [dB]
1	BL-1	25	1.5	1 000	0.00260	51.70
2	BL-1	50	3.0	2 000	0.00722	42.82
3	BL-1	75	4.5	3 000	0.02390	32.43
4	BL-1	100	6.0	4 000	0.04540	26.86
5	BL-2	25	3.0	3 000	0.00337	49.44
6	BL-2	50	1.5	4 000	0.00371	48.60
7	BL-2	75	6.0	1 000	0.00312	50.12
8	BL-2	100	4.5	2 000	0.02335	32.63
9	BL-3	25	4.5	4 000	0.00581	44.72
10	BL-3	50	6.0	3 000	0.01397	37.10
11	BL-3	75	1.5	2 000	0.00353	49.05
12	BL-3	100	3.0	1 000	0.00534	45.45
13	BL-4	25	6.0	2 000	0.00403	47.89
14	BL-4	50	4.5	1 000	0.00254	51.90
15	BL-4	75	3.0	4 000	0.00413	47.68
16	BL-4	100	1.5	3 000	0.00938	40.55

by calculating the average of wear responses of test run 1, 2, 3 and 4, which all involve BL-1 level of composition (see Table 3):

$$\text{Mean of means for BL-1} = \frac{0.0026 + 0.00722 + 0.0239 + 0.0454}{4} = 0.01978, \tag{22}$$

$$\text{Mean of means for BL-4} = \frac{0.00403 + 0.00254 + 0.00413 + 0.00938}{4} = 0.00502. \tag{23}$$

Similarly, the mean of means value for level IV (4 000 m) of sliding distance is obtained by calculating the average of wear responses of test run 4, 6, 9 and 15 as:

$$\text{Mean of means for 4 000 m} = \frac{0.0454 + 0.00371 + 0.00581 + 0.00413}{4} = 0.01476. \tag{24}$$

3. Results

The experimental results were analyzed using the Taguchi method, and the combination of control parameters and the most significant parameter affecting manufactured composite wear are identified. Table 3 shows that the change in composition, normal load, sliding velocity, and sliding distance much influenced the wear. Generally, the lowest weight loss of 0.00254 g was observed for composite BL-4 at 50 N normal load, 4.5 m/s sliding velocity and 1 000 m distance. The highest weight loss was observed for composite BL-1 at 100 N load, 6 m/s sliding speed with 4 000 m distance, and the order of 0.0454 g. It has been known that the highest SNR level is the optimal level for the control parameter. From Fig. 1, the optimal combination of the control parameter for wear is determined as A4 (BL-4 composition), B1 (25 N normal load), C1 (1.5 m/s sliding velocity) and D1 (1 000 m sliding distance). The corresponding plot for mean of means for wear is presented in Fig. 2. From the Fig. 1 and Fig. 2, it can be observed that the SNR response of wear increases (Fig. 1) with

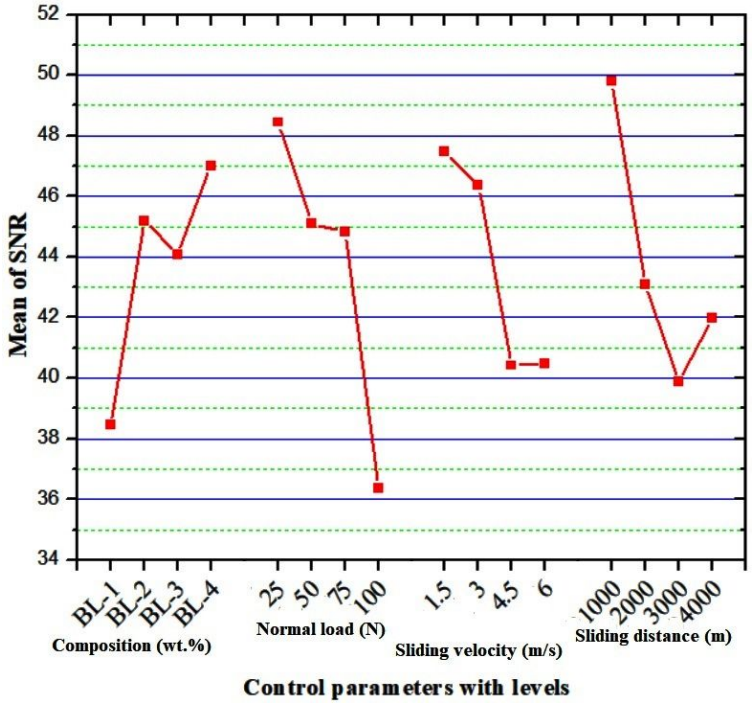

Figure 1. Main effect plot for mean of SNR

the inclusion of increased banan fiber content with corresponding decrease in lapinus fiber content, implying that the means (Fig. 2) of wear decrease. From Fig. 1, it can observed that SNR response decreases with increase in normal load, sliding distance and sliding velocity values. This decrease in SNR indicating that the wear of the composites increases gradually with an increase in normal load, sliding velocity and sliding distance. The wear observed decreased with increasing soft, i.e. banana fiber, and increased with hard lapinus fiber. For BL-1 composite, the amount of soft fiber is low

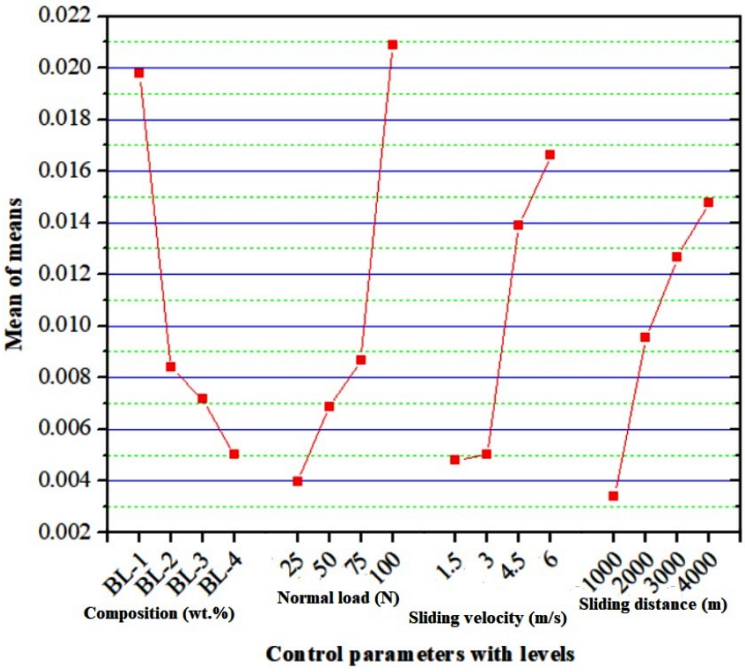

Figure 2. Main effect plot for mean of means

Table 4. Contribution ratio results

Control Parameter	$\overline{SNR}$	$\overline{\omega_i}$	$\overline{\omega}$	Δ_i
Composition [wt.%]	43.68	40.85	217.69	18.77
Normal load [N]		79.44		36.49
Sliding velocity [m/s]		42.37		19.46
Sliding distance [m]		55.03		25.28

(2.5 wt.%), while the higher amount of hard ingredients (nearly 27.5 wt.%) easily detached from the composite surface due to frictional heat generated during sliding resulted in increased wear. While in the case of BL-4 composite having nearly 20 wt.% of lapinus fiber, a higher amount of soft banana fiber (10 wt.%) was exposed on the surface that helps in reducing the wear of the composites [15]. The obtained trend for SNR and the mean of means graph are correlated to how they are calculated. The mean of means value was the average wear value for each level of each control parameter. Whereas the SNR is calculated using Fig. 2. In the Taguchi approach, a measure of robustness is used to identify control parameters that reduce variability in a process by minimizing the effects of uncontrollable factors such as noise that cannot be controlled during product design. The fluctuations in the SNR represent the experimental variation/error due to uncontrolled noise. Using the Taguchi approach, one can handle noise factors and determine the optimal parameter settings that minimize the effects of the noise [21].

Further the effectiveness of control parameters was analyzed in terms of contribution ratio as described in Table 4 and presented in Eq. (8-21). The order of the parametric usefulness for wear was normal load > sliding distance > sliding velocity > composition. The result reveals that normal load has the most dominant influence on wear with a percentage contribution of 36.49%, followed by sliding distance and sliding velocity with 25.28% and 19.46%, respectively. While composition has the lowest influence with a percent contribution of 18.77%.

4. Conclusions

Dry sliding wear response of banana and lapinus fiber reinforced brake friction composite materials under varying conditions of load, sliding velocity and sliding distance was successfully analyzed using Taguchi's experimental design method on a pin-on-disc machine. Results revealed that the composition of 10 wt.% banana fiber, 20 wt.% of lapinus fiber at 25 N load, 1.5 m/s sliding velocity and 1 000 m of sliding distance exhibit the lowest wear. It was also concluded that normal load primarily influences wear with a contribution of 36.49%, followed by sliding distance and sliding velocity with 25.28% and 19.46%, respectively. While composition have a minor influence on wear with a contribution of 18.77%.

5. References

[1] T. Singh, *Utilization of cement bypass dust in the development of sustainable automotive brake friction composite materials*, Arabian Journal of Chemistry 14, 2021, no. 103324. CrossRef

[2] T. Singh, *A hybrid multiple-criteria decision-making approach for selecting optimal automotive brake friction composite*, Material Design & Processing Communications 3, 2021, no. e266. CrossRef

[3] F. Ahmadijokani, A. Shojaei, S. Dordanihaghighi, E. Jafarpour, S. Mohammadi, M. Arjmand, *Effects of hybrid carbon-aramid fiber on performance of non-asbestos organic brake friction composites*, Wear 452-453, 2020, no. 203280. CrossRef

[4] A. Tiwari, H.S. Jaggi, R.K. Kachhap, B.K. Satapathy, S.N. Maiti, B.S. Tomar, *Comparative performance assessment of cenosphere and barium sulphate based friction composites*, Wear 309, 2014, pp. 259-268. CrossRef

[5] J. Bijwe, N.N. Majumdar, B.K. Satapathy, *Influence of modified phenolic resins on the fade and recovery behavior of friction materials*, Wear 259, 2005, pp. 1068- 1078. CrossRef

[6] M.H. Cho, J. Ju, S.J. Kim, H. Jang, *Tribological properties of solid lubricants (graphite, Sb2S3, MoS2) for automotive brake friction materials*, Wear 260, 2006, pp. 855-860. CrossRef

[7] T. Singh, A. Patnaik, *Thermo-mechanical and tribological properties of multi-walled carbon nanotubes filled friction composite materials*, Polymer Composites 38, 2017, pp. 1183-1193. CrossRef

[8] T. Singh, *Optimum design based on fabricated natural fiber reinforced automotive brake friction composites using hybrid CRITIC-MEW approach*, Journal of Materials Research and Technology 14, 2021, pp. 81-92. CrossRef

[9] P. Monreal, I. Clavería, P. Arteta, T. Rouzaut, *Effect of modified novolac resins on the physical properties and friction performance of railway brake blocks*, Tribology International 154, 2021, no. 106722. CrossRef

[10] K. Malachova, K. Jana, R. Zuzana, S. Hana, P. Daniela, C. Kristina, F. Peter, *Toxicity and mutagenicity of low-metallic automotive brake pad materials*, Ecotoxicology and Environmental Safety 131, 2016, pp. 37-44. CrossRef

[11] T. Singh, P. Pattnaik, C.I. Pruncu, A. Tiwari, G. Fekete, *Selection of natural fibers based brake friction composites using hybrid ELECTRE-entropy optimization technique*, Polymer Testing 89, 2020, no. 106614. CrossRef

[12] T. Singh, C.I. Pruncu, B. Gangil, V. Singh, G. Fekete, Comparative performance assessment of pineapple and Kevlar fibers based friction composites, Journal of Materials Research and Technology 9, 2020, pp. 1491-1499. CrossRef

[13] B.S. Rajan, M.A. Saibalaji, S.R. Mohideen, *Tribological performance evaluation of epoxy modified phenolic FC reinforced with chemically modified Prosopis juliflora bark fiber*, Materials Research Express 6, 2019, no. 075313. CrossRef

[14] M.J. Ahmed, M.A.S. Balaji, S.S. Saravanakumar, M.R. Sanjay, P. Senthamaraikannan, *Characterization of Areva javanica fiber - A possible replacement for synthetic acrylic fiber in the disc brake pad*, Journal of Industrial textiles 49, 2019, pp. 294-317. CrossRef

[15] T. Singh, A. Patnaik, *Performance assessment of lapinus-aramid based brake pad hybrid phenolic composites in friction braking*, Archives of Civil and Mechanical Engineering 15, 2015, 151-161. CrossRef

[16] N. Dadkar, B.S. Tomar, B.K. Satapathy, A. Patnaik, *Performance assessment of hybrid composite friction materials based on fly ash-rock fibre combination*, Materials and Design 31, 2010, 723-731. CrossRef

[17] T. Singh, B. Gangil, B. Singh, S.K. Verma, D. Biswas, G. Fekete, *Natural-synthetic fiber reinforced homogeneous and functionally graded vinylester composites: Effect of bagasse-Kevlar hybridization on wear behaviour*, Journal of Materials Research and Technology 8, 2019, pp. 5961-5971. CrossRef

[18] M.A. Abdelgnei, M.Z. Omar, M.J. Ghazali, M.N. Mohammed, B. Rashid, *Dry sliding wear behaviour of thixoformed Al-5.7Si-2Cu-0.3 Mg alloys at high temperatures using Taguchi method*, Wear 442-443, 2020, no. 203134. CrossRef

[19] O. Hussain, S.S. Saleem, B. Ahmad *Friction and wear performance evaluation of UHMWPE using Taguchi based grey approach: A study on the influence of load and bio-serum lubrication*, Materials Chemistry and Physics 239, 2020, no. 121918. CrossRef

[20] R. Chauhan, T. Singh, N. Kumar, A. Patnaik, N.S. Thakur, *Experimental investigation and optimization of impinging jet solar thermal collector by Taguchi method*, Applied Thermal Engineering 116, 2017, pp. 100-109. CrossRef

[21] D.C. Montgomery, *Design and analysis of experiments*, John Wiley & Sons, Inc. ISBN 978-1-119-49244-3

EÖTVÖS LORÁND UNIVERSITY
FACULTY OF INFORMATICS
SAVARIA INSTITUTE OF TECHNOLOGY

www. szombathelyigepesz.hu